

THE INVISIBLES: A DETECTION ALGORITHM TO TRACE THE FAINTEST MILKY WAY SATELLITES

S. M. WALSH¹, B. WILLMAN², H. JERJEN¹

Draft version July 21, 2021

ABSTRACT

A specialized data mining algorithm has been developed using wide-field photometry catalogues, enabling systematic and efficient searches for resolved, extremely low surface brightness satellite galaxies in the halo of the Milky Way (MW). Tested and calibrated with the Sloan Digital Sky Survey Data Release 6 (SDSS-DR6) we recover all fifteen MW satellites recently detected in SDSS, six known MW/Local Group dSphs in the SDSS footprint, and 19 previously known globular and open clusters. In addition, 30 point source overdensities have been found that correspond to no cataloged objects. The detection efficiencies of the algorithm have been carefully quantified by simulating more than three million model satellites embedded in star fields typical of those observed in SDSS, covering a wide range of parameters including galaxy distance, scale-length, luminosity, and Galactic latitude. We present several parameterizations of these detection limits to facilitate comparison between the observed Milky Way satellite population and predictions. We find that all known satellites would be detected with $> 90\%$ efficiency over all latitudes spanned by DR6 and that the MW satellite census within DR6 is complete to a magnitude limit of $M_V \approx -6.5$ and a distance of 300 kpc. Assuming all existing MW satellites contain an appreciable old stellar population and have sizes and luminosities comparable to currently known companions, we predict lower and upper limit totals of 52 and 340 Milky Way dwarf satellites within ~ 260 kpc if they are uniformly distributed across the sky. This result implies that many MW satellites still remain undetected. Identifying and studying these elusive satellites in future survey data will be fundamental to test the dark matter distribution on kpc scales.

Subject headings: dark matter, dwarf galaxies, Local Group

1. INTRODUCTION

The dwarf galaxy population of the Milky Way (MW) provides invaluable insight into galaxy formation and evolution. Their resolved stars reveal their formation histories and enable precise measurements of their structural parameters, ages and metallicities. These histories of individual, nearby systems provide a unique approach to studying the Universe across the cosmic ages. Dwarf galaxies are also the most numerous type of galaxy in the Universe and are thought to be the building blocks of larger galaxies. Owing to their low masses, their properties may be strongly influenced by ionizing radiation in the early Universe and by the energy released by supernovae. The impacts of both of these are weak links in our understanding of structure formation. Finding and studying nearby dwarfs of the lowest masses and luminosities is thus an essential component to understanding galaxy formation on all scales.

The Milky Way dwarf galaxy population is also at present the most direct tracer of the abundance, mass spectrum, characteristic size, and spatial distribution of dark matter on sub-galactic scales. Standard Λ CDM simulations of MW-size dark matter haloes predict many more dark matter sub-haloes than are observed as dwarf galaxies (Klypin et al. 1999; Moore et al. 1999). The recent “Via Lactea” simulation contains 2,000 dark matter sub-halos within 289 kpc of the simulated primary galaxy (Diemand et al. 2007) which have no observed optically luminous counterparts. This discrepancy gives rise to the

questions how and in what mass regime do the baryons disappear from dark matter clumps? Studies of the spatial distributions of Milky Way and M31 dwarf galaxy companions have also highlighted possible discrepancies between Λ CDM theory and observations (Kroupa et al. 2005; Kang et al. 2005; Metz et al. 2007).

The most obvious reason for these apparent discrepancies in the number and spatial distributions of dwarf galaxies is substantial incompleteness as the Milky Way halo has not yet been uniformly searched for dwarf galaxy companions to low enough luminosities and star densities, in particular close to the Galactic plane where foreground contamination is severe. For example, Willman et al. (2004) compared the spatial distribution of MW satellites to that of M31’s population, as well as that of a simulated dark matter halo and concluded that some dwarfs may have been missed at low Galactic latitudes, and that the total number of MW satellites with properties similar to the known objects could be as many as triple the known population.

The viability of this solution, at least in part, has been underscored by the recent discoveries of fourteen new Galactic companions from the photometric data of the Sloan Digital Sky Survey (SDSS). These objects all appear to be dominated by old ($\gtrsim 10$ Gyr) stellar populations, with the exception of Leo T (de Jong et al. 2008). Nine of these companions were immediately identified as dwarf spheroidal (dSph) galaxies: Ursa Major, Canes Venatici, Boötes, Ursa Major II, Canes Venatici II, Hercules, Leo IV, Coma Berenices, Leo T and Leo V (Willman et al. 2005b; Zucker et al. 2006b; Belokurov et al. 2006b; Zucker et al. 2006a; Belokurov et al. 2007; Irwin et al. 2007; Belokurov et al.

¹ Research School of Astronomy and Astrophysics, Australian National University, Cotter Road, Weston, ACT 2611;

² Clay Fellow, Harvard-Smithsonian Center for Astrophysics, 60 Garden Street Cambridge, MA 02138

2008). Spectroscopic follow-up has confirmed that they all are highly dark matter dominated dwarf galaxies (Simon & Geha 2007; Martin et al. 2007). Willman 1, Segue 1 and Boötes II (Willman et al. 2005a; Belokurov et al. 2007; Walsh et al. 2007a) occupy a region of size-luminosity space not previously known to be inhabited by old stellar populations, at the intersection of MW dSphs and globular clusters. Spectroscopic studies (Martin et al. 2007) showed that Willman 1 may be resident inside a dark matter subhalo with a mass-to-light ratio of ~ 470 . If these ambiguous objects are gravitationally bound, then tidal arguments also favor them being dark matter dominated (Walsh et al. 2007b). The remaining two objects discovered in SDSS, Kuposov 1 and 2, (Kuposov et al. 2007b) are extremely faint Galactic globular clusters.

Numerous authors have shown that the predictions of Λ CDM simulations can be reconciled with the small number of observed MW dwarf galaxies if simple models for baryonic physical processes are taken into account when interpreting the results of numerical simulations (e.g. Bullock et al. 2001; Kravtsov et al. 2004; Simon & Geha 2007). For example, Strigari et al. (2007) show that the central masses ($M_{0.6kpc}$) of the Milky Way dwarf galaxies are well-constrained by the data and that their mass function closely matches the $M_{0.6kpc}$ mass function of both the earliest forming sub-halos and the most massive accreted sub-halos in the Via Lactea simulation.

A well-defined, deep survey of Milky Way dwarf galaxies over a large fraction of the sky is critical to assess any of the above scenarios. The dwarf galaxies detected (or not) by such a survey will provide one of the best ways to rigorously test the Λ CDM paradigm by comparing a variety of metrics (distribution, mass, scale sizes, and number) of the Milky Way dwarfs with the predictions of Λ CDM + galaxy formation models. Willman et al (2002) and Kuposov et al. (2007a) have previously conducted automated searches for Milky Way dwarfs in the SDSS and their corresponding detection limits. The original Willman et al survey was only performed over a couple of thousand square degrees of sky. The Kuposov et al. (2007a) survey was performed with a more sensitive algorithm (critical, because they found many new satellites to be on the edge of detectability), but few galaxies were used to accurately quantify their detection limits.

In this paper, we present critical improvements to the present characterization of the detectability of Milky Way dwarf galaxies over the $\sim 9,500$ square degrees of the SDSS in Data Release 6 (DR6). We also present an improved detection algorithm over previous searches. We aim to construct the most complete, well-defined census of MW satellites by embarking on a Milky Way all sky satellite hunt. This search will ultimately combine SDSS Data Release 6 (Adelman-McCarthy et al. 2008), The 2-Micron All Sky Survey (2MASS; Skrutskie et al. 2006) and the upcoming Southern Sky Survey (Keller et al. 2007). The Southern Sky Survey will cover the entire $20,000 \text{ deg}^2$ below $\delta < 0^\circ$ using the new Australian National University (ANU) SkyMapper Telescope equipped with a 5.7 sq degree wide-field camera that is currently under construction with survey operation expected to commence early 2009.

2. SDSS DATA

The Sloan Digital Sky Survey (York et al. 2000) is an automated multi-color imaging and spectroscopic survey spanning 9,500 square degrees surrounding the North Galactic Pole. The u, g, r, i and z imaging data (Fukugita et al. 1996; Gunn et al. 1998) are photometrically and astrometrically reduced through an automatic pipeline (Hogg et al. 2001; Ivezić et al. 2004; Smith et al. 2002; Tucker et al. 2006; Pier et al. 2003). We subsequently correct for reddening with the Schlegel et al. (1998) extinction values given in the SDSS catalog. All following work is performed on point sources from DR6, using the photometry flags from the examples of database queries appropriate for point sources available on the SDSS Skyserver website³. To ameliorate effects of incompleteness in the point source catalog and star/galaxy separation, we only consider sources brighter than $r = 22.0$. The photometric data are provided by the SDSS DR6 (Adelman-McCarthy et al. 2008). We take our data from local copies of the SDSS datasets, maintained at the Harvard-Smithsonian Center for Astrophysics.

3. SURVEY METHOD

Low surface brightness Milky Way satellites are detectable only by their resolved stars. With the least luminous known Milky Way satellites, such as Boötes II, containing fewer than ~ 20 stars brighter than the main sequence turn-off (Walsh et al. 2007b), a deep, wide-field, uniform, multi-color photometric catalog is essential for searching for these objects. They will typically reveal their presence as statistically significant spatial overdensities relative to the Galactic foreground. Their signal can be enhanced by selecting stellar sources that are consistent in color-magnitude space with, for example, an old population of stars at a fixed distance. In this paper, we restrict ourselves to the old stellar populations characteristic of Local Group dSphs, but the population-specific elements of the algorithm can be easily modified for other systems. The strategy of our detection algorithm is built upon that of Willman et al. (2002) and Willman (2003) which utilized the photometric catalogs from SDSS and led to the discoveries of Ursa Major (Willman et al. 2005b) and Willman 1 (Willman et al. 2005a). It is also similar in spirit to Belokurov et al. (2007) and Kuposov et al. (2007a). Several systematic searches for MW dwarfs have also been done with non-SDSS data (Irwin 1994; Kleyrna et al. 1997; Whiting et al. 2007).

In summary, our algorithm applies color and magnitude cuts to stars in the DR6 catalog, stores their distribution in a spatial array with $0.02^\circ \times 0.02^\circ$ pixels, spatially smooths the array with a Plummer surface density profile, and sets comprehensive thresholds for detection. Each of these steps is described in detail in the following sections.

3.1. Data Management

In order to efficiently manage thousands of square degrees of survey data in a catalog containing tens of millions of stars, we first divide the dataset (in the case

³ <http://cas.sdss.org/dr6/>

discussed in this paper, SDSS DR6) into stripes, each spanning 3° in declination (to avoid projection effects) with 2° of overlap in Dec between adjacent stripes. This overlap creates a substantial redundancy to ensure that real objects are situated in the central $\sim 2^\circ$ of Declination in at least one stripe, away from possible edge-effects introduced at the stripe boundaries during the processing described in §3.3. We then take the longest continuous regions of the DR6 footprint in RA.

3.2. Selection Criteria

The mainly old, metal-poor stars of a nearby dwarf galaxy will occupy a well defined locus in the color-magnitude diagram (CMD), in contrast to Milky Way stars which span a wide range in distance, age, and metallicity. Therefore selecting stars that are consistent in color-magnitude space with a population of old stars at a particular distance will significantly enhance the clustering contrast of a dwarf galaxy’s stars over the foreground noise from Milky Way stars.

We use theoretical isochrones in SDSS filters from Girardi et al. (2004) to define the regions of $(r, g - r)$ space likely to be populated by old, metal-poor stars. Simon & Geha (2007) obtained spectra of stars in eight of the newly discovered dwarfs: CVn, CVn II, Com, Her, Leo IV, Leo T, UMa and UMa II and found mean abundances in the range $-2.29 < [\text{Fe}/\text{H}] < -1.97$. Based on this result, we consider isochrones for populations with abundances of $[\text{Fe}/\text{H}] = -1.5$ and -2.27 (the lower limit in Girardi et al. 2004) and with ages 8 and 14 Gyr. Four isochrones in these ranges can be used to bound the region of CMD space we are interested in, namely the four combinations of $[\text{Fe}/\text{H}] = -1.5$ and -2.27 and ages 8 and 14 Gyr. Figure 1 shows these four isochrones projected to a distance of 20 kpc.

We define the selection criteria by the CMD envelope inclusive of these isochrones \pm the 1 sigma $(g - r)$ color measurement error as a function of r magnitude. Shifting these isochrones over distances between $m - M = 16.5 - 24.0$ in 0.5 mag steps defines 16 different selection criteria appropriate for old stellar populations between $d \sim 20$ kpc and $\gtrsim 630$ kpc. We truncate our color-magnitude selection template at a faint magnitude limit of $r = 22.0$, beyond which photometric uncertainties in the colors and star/galaxy separation limit the ability to detect these populations. We also truncate the selection template at $g - r = 1.0$ as including redder objects adds more noise from Milky Way dwarf stars than signal from more distant red giant branch (RGB) stars. Finally we do not include stars with δg or $\delta r > 0.3$ mag in our analysis. To efficiently select stars within this CMD envelope, we treat the CMD as an image of 0.025×0.125 (color \times mag) pixels and determine which stars fall into pixels classified as “good” according to the selection criteria. Figure 1 shows an example of the selection criteria, in this case for $m - M = 16.5$ (~ 20 kpc). The shaded region highlights pixels that would be classed as “good” for a system at ~ 20 kpc.

3.3. Spatial Smoothing

After the photometric cuts are applied, we bin the spatial positions of the selected stars into an array, E , with $0.02^\circ \times 0.02^\circ$ pixel size. We then convolve this

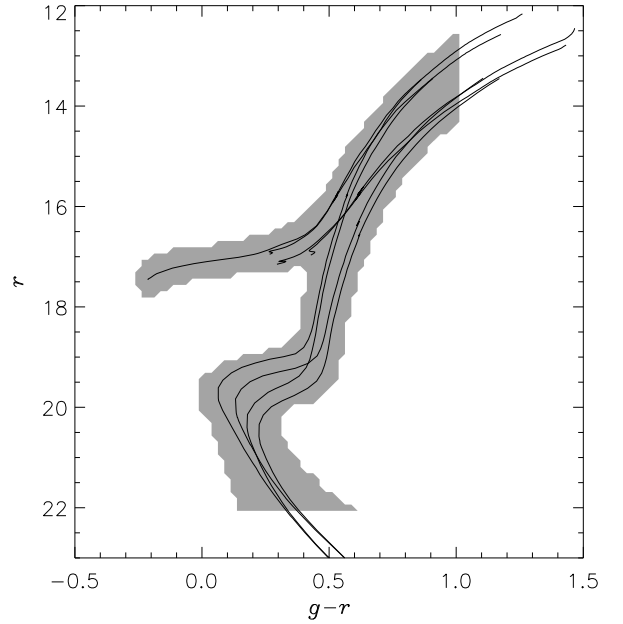


FIG. 1.— $(r, g - r)$ color-magnitude diagram showing the two redder and two bluest theoretical isochrones for old stellar populations ($[\text{Fe}/\text{H}] = -2.27, -1.5$ and age 8, 14 Gyr) at a distance modulus of $m - M = 16.5$ (~ 20 kpc), generated from Girardi et al. (2004). The shaded region shows pixels that pass the selection criteria.

TABLE 1
ANGULAR SIZES OF THE
SATELLITES DETECTED IN
SDSS.

Object	r_h (arcmin)
Boötes	12.6
Boötes II	4.2
Canes Venatici	8.9
Canes Venatici II	1.6
Coma Berenices	6.0
Hercules	8.6
Leo IV	2.5
Leo V	0.8
Leo T	1.4
Segue 1	4.4
Ursa Major	11.3
Ursa Major II	16.0
Willman 1	2.3

2D array with a spatial kernel corresponding to the expected surface density profile of a dSph. We refer to this smoothed spatial array as A . For our spatial kernel we use a Plummer profile with a $4.5'$ scale-length. This value provides an effective compromise between the angular scale-lengths of compact and/or distant objects with those of closer/more extended objects. For reference the angular sizes of the new satellites are listed in Table 1. We use the r_h values derived by Martin et al. (2008) except for Leo V (Belokurov et al. 2008).

The normalized signal in each pixel of A , denoted by S , gives the number of standard deviations above the local

mean for each element:

$$S = \frac{A - \bar{A}}{A_\sigma}.$$

The arrays of running means, \bar{A} , and running standard deviations, A_σ are both calculated over a $0.9^\circ \times 0.9^\circ$ window around each pixel of A . In particular, A_σ is given by:

$$A_\sigma = \sqrt{\frac{n(A - \bar{A})^2 * B - ((A - \bar{A}) * B)^2}{n(n - 1)}}.$$

B is a box-filter with n elements and is the same size as the running average window. The resulting array A_σ gives the standard deviation value for each pixel of A as measured over the $0.9^\circ \times 0.9^\circ$ span of the filter. In the next section, we will define the detection threshold of this survey in terms of S , as well as in terms of the local stellar density E .

3.4. Detection Threshold(s)

In a large survey such as ours, it is critical to set detection thresholds strict enough to eliminate false detections but loose enough to retain known objects and promising candidates. To characterize the frequency and magnitude of truly random fluctuations in stellar density analyzed with our algorithm, we measure the maximum value of S for 199,000 $5.5^\circ \times 3^\circ$ simulated fields of randomly distributed stars that have been smoothed as described in the previous section. The only difference is that there is no gradient in stellar density across each field. In the interest of computational efficiency we do not use a running window for the mean and σ of each simulated field. The field size is chosen such that 1,000 fields roughly totals an area equal to the DR6 footprint (neglecting regions lost during convolution). We select 199 stellar densities n_* to simulate, linearly spaced between 10 and 4,000 stars per square degree. This range of stellar densities is to model the density range we find *after* applying the color-magnitude selection criteria described in §3.2 across the SDSS. In §5.1 we study the variation of detection limits with Galactic latitude (foreground stellar density); the typical number densities we will consider there are higher than 10 - 4,000 stars per square degree because we wish to parametrize the detection limits in terms of the density of *all* stars bluer than $g - r = 1.0$ and brighter than $r = 22$.

Figure 2 shows a two dimensional cumulative histogram of the 199,000 $\max(S)$ values as a function of stellar density. In low density fields, the distribution of pixel values becomes non-Gaussian so a simple, global threshold value is insufficient. The solid grey line shows the contour containing 99% of the 199,000 $\max(S)$ values at each density. If we simply used a value like this as our threshold, we would be biasing ourselves against detecting extended objects: Large angular scale-length systems may not have a peak pixel value above this value, for example because stars in the object itself increases the local running mean and sigma. However, such an overdensity may have a characteristic area larger than any random fluctuation.

We thus define a detection threshold based on both the peak density and the characteristic area of an overden-

sity. To define such an area we scale down the 99% contour from Figure 2 and define a threshold density $S_{th}(n_*)$ as a function of stellar number density. Then, using the 199,000 random fields we examine the relationship between the peak density $\max(S)$ divided by $S_{th}(n_*)$ and “detection” area, i.e. the area of contiguous pixels of S that have values above $S_{th}(n_*)$ (the white line). Figure 3 shows this area versus $\max(S)/S_{th}(n_*)$ for the random fields. If we assume a purely random foreground, we would expect one false detection in the DR6 footprint above an area of ~ 55 square arcminutes *or* above a peak density of $\sim 1.6 \times S_{th}(n_*)$. These numbers are set by the factor by which we scale down the threshold function and are themselves arbitrary.

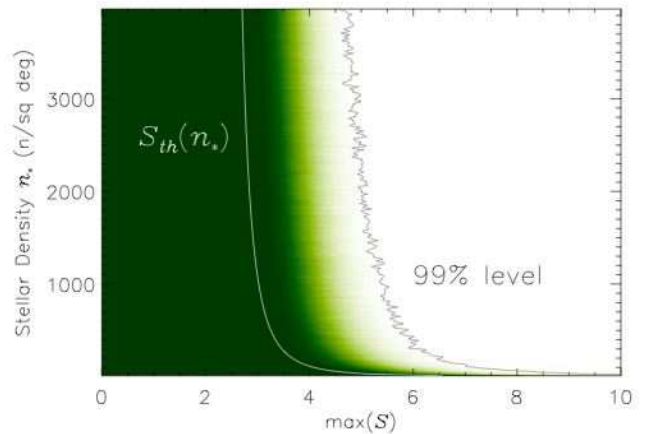


FIG. 2.— A two dimensional cumulative histogram showing the distribution of $\max(S)$ values for smoothed fields as a function of different stellar densities n_* . The grey line bounds 99% of the $\max(S)$ values and the white line shows our threshold density, $S_{th} = f(n_*)$.

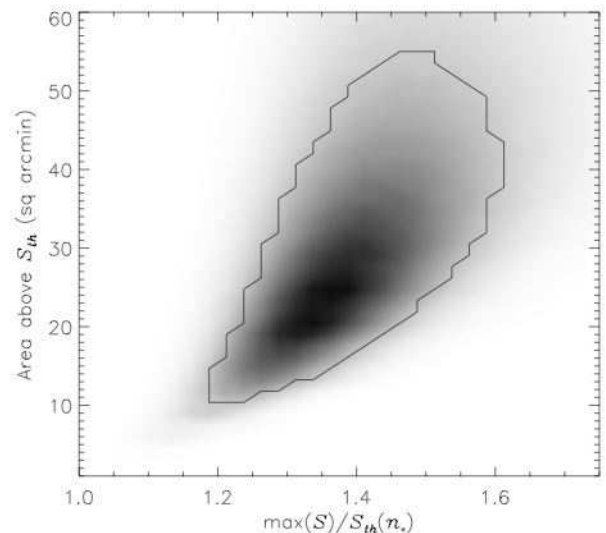


FIG. 3.— “Detection” area versus $\max(S)/S_{th}(n_*)$ for the 199,000 random fields. The black contour shows the level at which purely random clustering would produce one false detection over the approximate area of DR6.

Based on the results of these simulations we set the

area threshold to a more conservative 60.0 sq arcmin and the density threshold to a more conservative $1.75 \times S_{th}(n_*)$ to eliminate false positive fluctuations while preserving all of the known objects within DR6, including Boötes II (Walsh et al. 2007a) and the Koposov 1 and 2 globular clusters (Koposov et al. 2007b). Thus, a detection is defined as a region where:

- the area of a group of pixels of S contiguously above $S_{th}(n_*)$ (white line, Fig 2) is greater than 60.0 square arcminutes
or
- any single pixel value is greater than $1.75 \times S_{th}(n_*)$.

We implement these adaptive density thresholds as a function of local stellar density n_* , so that the algorithm may be run over large fields with varying density and allow direct comparison between fields of greatly different densities. The stellar density n_* is calculated for each pixel of the smoothed, normalized, spatial array S , as the $0.9^\circ \times 0.9^\circ$ running average of the original spatial density array E .

To summarize our algorithm:

- Apply CMD cuts, bin spatial positions of remaining stars into E
- Smooth E with Plummer profile to get A
- Calculate the $0.9^\circ \times 0.9^\circ$ running mean \bar{A} and running standard deviation A_σ
- Define S as $S = (A - \bar{A})/A_\sigma$
- Calculate array of threshold values S_{th} as function of stellar density n_* (from $0.9^\circ \times 0.9^\circ$ running mean of E)
- Detections are where contiguous regions of pixels with $S > S_{th}$ is greater than 60.0 sq arcmin or any single pixel is greater than $1.75 \times S_{th}$.

3.5. Identifying and Evaluating Detections

For each of our DR6 data strips defined in §3.1, the steps outlined in the previous sections are repeated in 0.5 magnitude distance modulus intervals, and these 16 frames are layered to form a 3-dimensional array. This 3D approach eliminates complications with multiple detections of a single object using selection criteria for different distance moduli, and selects out the strongest detection. The coordinates of stars within each detection and the CMD within the detection’s area are plotted for later visual inspection. Galaxy clusters and point sources around partially resolved background galaxies (such as their associated globular clusters) will contaminate the detections, but these can be identifiable based on their CMDs (see Figure 9 in §4), leaving a list of potential new Milky Way satellite galaxies and globular clusters. At this point follow up observations are typically necessary to confirm the existence and nature of these candidates.

4. APPLICATION TO SDSS DATA RELEASE 6

We apply our search algorithm (as described in §3) to 21,439,777 sources with $r < 22.0$ and $g - r < 1.0$ in the 9,500 deg² of imaging data in Data Release 6 of the SDSS.

The DR6 footprint is shown in Figure 4, along with previously known dSphs (open blue circles) and satellites discovered in SDSS (closed red circles).

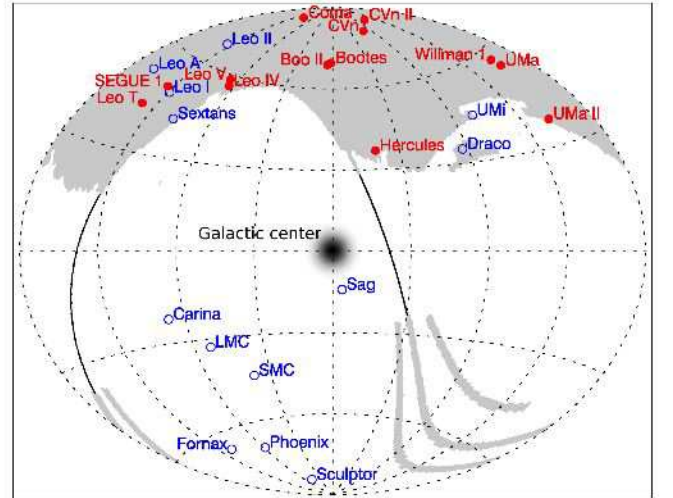


FIG. 4.— Aitoff projection of the DR6 footprint in Galactic coordinates, centered on the Galactic center. Previously known dwarfs are marked with open blue circles, satellites discovered in SDSS are marked with filled red circles.

The significance of our detections of known objects in terms of their peak density and area are shown in Figure 5. In the total area of DR6 analyzed, we find 100 unique detections above the thresholds, defined by the dotted lines of Figure 5. The positions of each of these detections are cross-referenced against the SIMBAD database⁴ as well as visually inspected via the SDSS Finding Chart Tool⁵. Of our 100 detections, 19 are MW/Local Group dwarfs (counting Boötes II, Willman 1 and Segue 1), 17 are Galactic globular clusters (including Koposov 1 and 2), 2 are known open clusters, 28 are clustering of point sources associated with background galaxies such as unresolved distant globular clusters, and four are Abell galaxy clusters. The remaining 30 do not correspond to any catalogued objects, but color-magnitude diagrams of only a handful of these are consistent enough with a faint MW satellite to warrant follow-up. The remainder may be galaxy clusters whose detected center differs from its cataloged centre by more than $\sim 0.25^\circ$, or perhaps tidal debris. If the MW stellar halo is the result of accretion of dSph then evidence of this accretion is expected. It should be noted that objects with relatively large angular size, such as Draco and Sextans, substantially increase the average stellar density of the area they occupy which increases the threshold density, meaning they are not as high above the density threshold as one might expect. Due to the area threshold however, they are still very prominent detections.

We recover all of the newly discovered objects that are within DR6 and the “classically” known Draco, Leo, Leo II, Leo A, Sextans, and Pegasus DIG dwarfs. Our detections of the new dwarfs are presented in Figures 6, 7, and

⁴ <http://simbad.u-strasbg.fr/simbad/>

⁵ <http://cas.sdss.org/astrodr6/en/tools/chart/chart.asp>

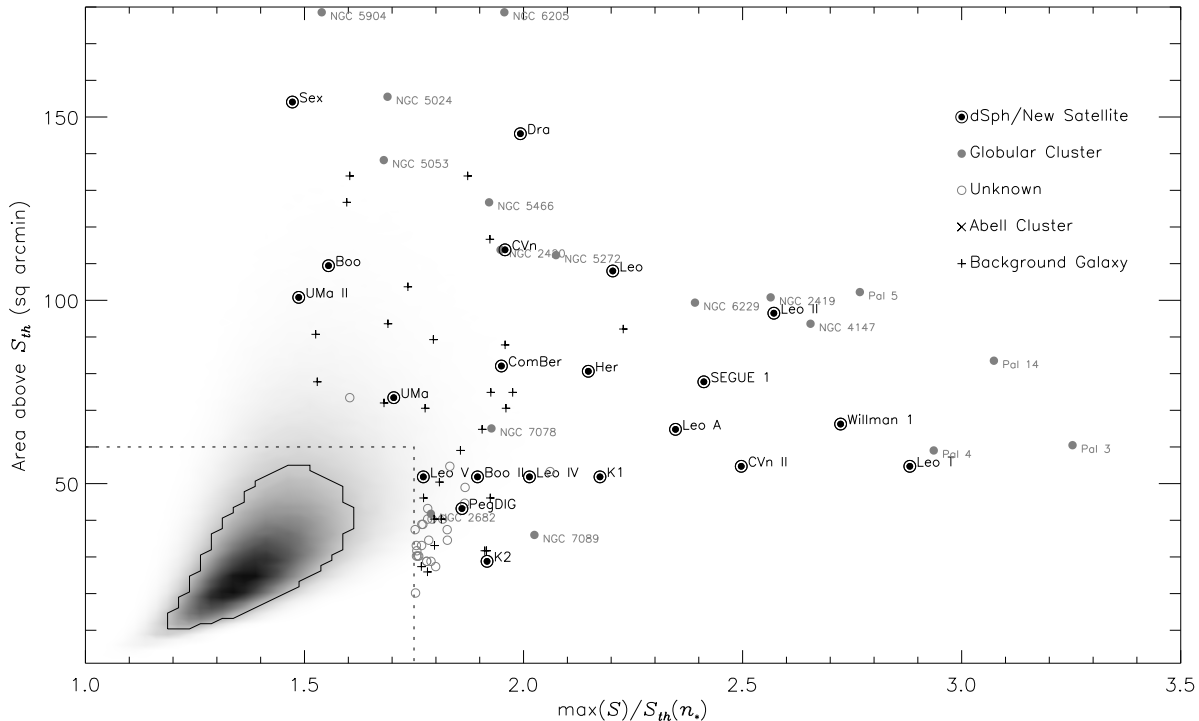


FIG. 5.— Same as Figure 3 but showing all detections in DR6. Dotted black lines show the adopted thresholds. Galactic/Local Group dSphs and Koposov 1 and 2 are shown as black filled circles. The brightest objects such as Draco and Sextans increase the average stellar density of the area they occupy, which increases $S_{th}(n_*)$ in their vicinity. This means that $\max(S)/S_{th}(n_*)$ is not as high as one might expect.

8. These figures are identical to those output by the automated algorithm for each detection, aside from the addition of figure titles (M_V and distances from Martin et al. 2008 and references therein). The left panel shows the spatial positions of stars passing the photometric selection criteria at the distance modulus the object was most strongly detected at. The middle-left panel shows the contour plot corresponding to S , where the contour levels are $(S)/S_{th}(n_*) = 1.0, 1.2, 1.4, 1.6, 1.8,$ and 2.0 . The middle-right panel is the CMD of the detection area and the right panel is the field subtracted Hess diagram. The isochrone is that of a 13 Gyr, $[\text{Fe}/\text{H}] = -2.3$ from Girardi et al. (2004) at the distance specified. Besides demonstrating the effectiveness of our algorithm, these detections provide a benchmark with which to compare candidates and determine which are consistent with being a new dwarf satellite.

To further illustrate the product of our algorithm we also show examples of undesired detections in Figure 9: the galaxy cluster Abell 1413 (top) and Virgo cluster galaxy NGC 4486 (bottom). These represent typical detections of background galaxies and galaxy clusters.

4.1. Candidate Milky Way Satellites

Figure 10 shows four unidentified overdensities that have CMDs qualitatively similar to that of a dSph. All show statistically significant spatial clustering and do not coincide with a visible overdensity of background galaxies. While several unknown detections have CMDs broadly consistent with old stellar populations, we present here four detections that are as strong or stronger than the detections of UMa and PegDIG. We

TABLE 2
POSITIONS OF STRONGEST MW SATELLITE CANDIDATES

Designation	α	δ	(α, δ)	D (kpc)
“CVn W”	13:16:04.8	+33:15:00	(199.02, 33.25)	~ 160
“Her X”	16:27:45.6	+29:27:00	(246.94, 29.45)	~ 100
“UMa Y”	12:11:57.6	+53:35:24	(182.99, 53.59)	~ 100
“Vir Z”	12:20:19.2	-1:21:00	(185.08, -1.35)	~ 40

present their positions and distances estimated from the CMD in Table 2.

5. EXPLORING DETECTION EFFICIENCY WITH SYNTHETIC SATELLITES

The most advantageous aspect of a large, uniform search for MW dwarfs is the ability to rigorously calculate its detection limits in order to compare observations with predictions. To calculate the detection completeness of our search, artificially generated galaxies are embedded in simulated stellar foreground fields and put through the detection algorithm to investigate the sensitivity as a function of galaxy distance, luminosity, scale-length, and Galactic latitude. In this section, we describe in detail the method used to synthesize artificial SDSS fields and dSph satellites.

5.1. Sowing the Simulated Fields

When simulating fields in which to embed artificial galaxies, our goal is to create a large number of fields with the same point source color, magnitude, and density distributions as observed in the SDSS DR6 footprint. The detectability of a dSph may change depending on its

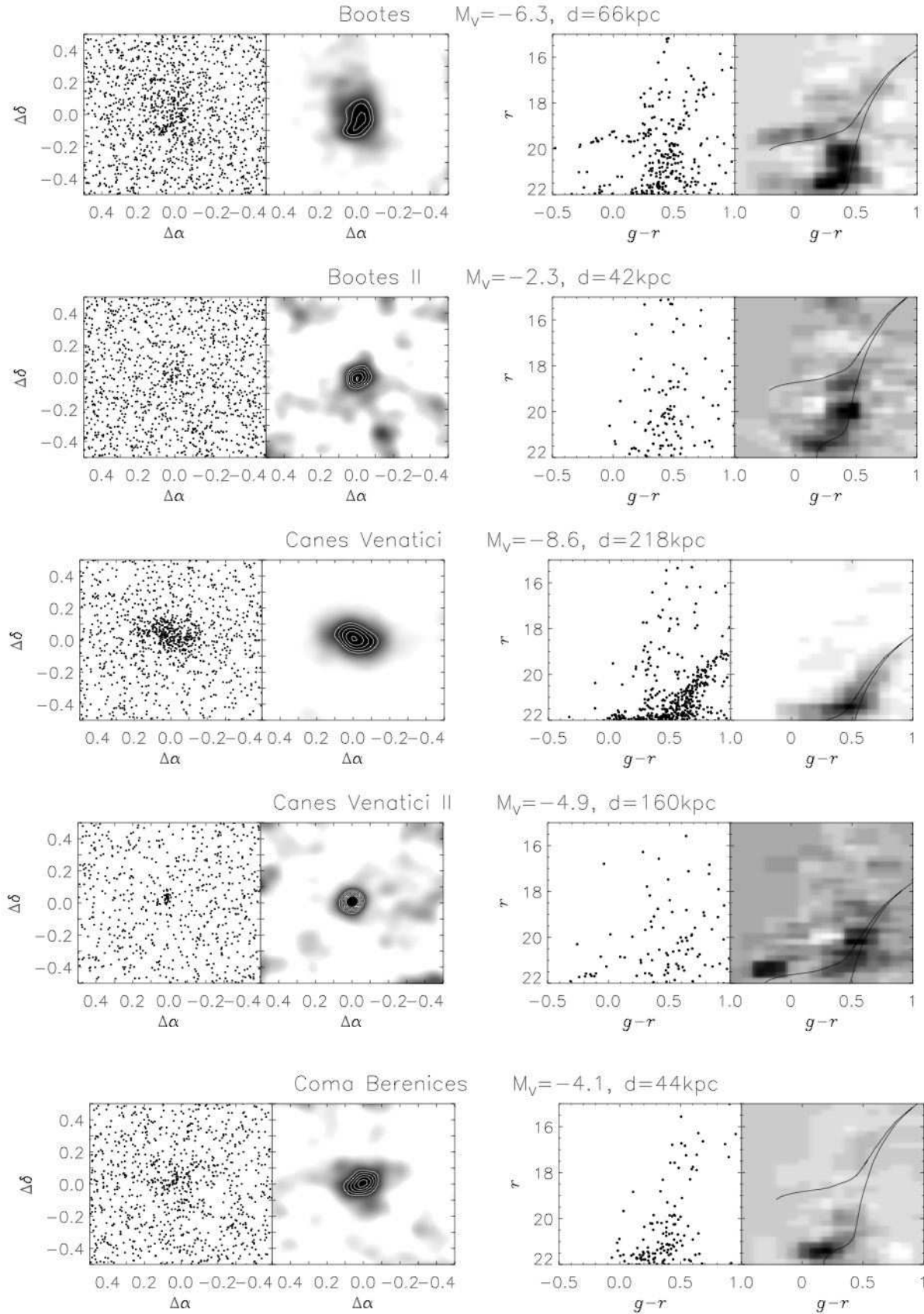


FIG. 6.— Our detections of recently discovered MW satellites. *Left:* Spatial plot of sources passing selection cut. *Middle Left:* Contour of smoothed spatial plot. Contours show 1.0, 1.2, 1.4, 1.6, 1.8, and 2.0 times the density threshold. *Middle Right:* CMD of region enclosed by contours. *Right:* Hess diagram of same region, with 13 Gyr, $[\text{Fe}/\text{H}] = -2.3$ Girardi et al. (2004) isochrone at the objects' distance overlotted.

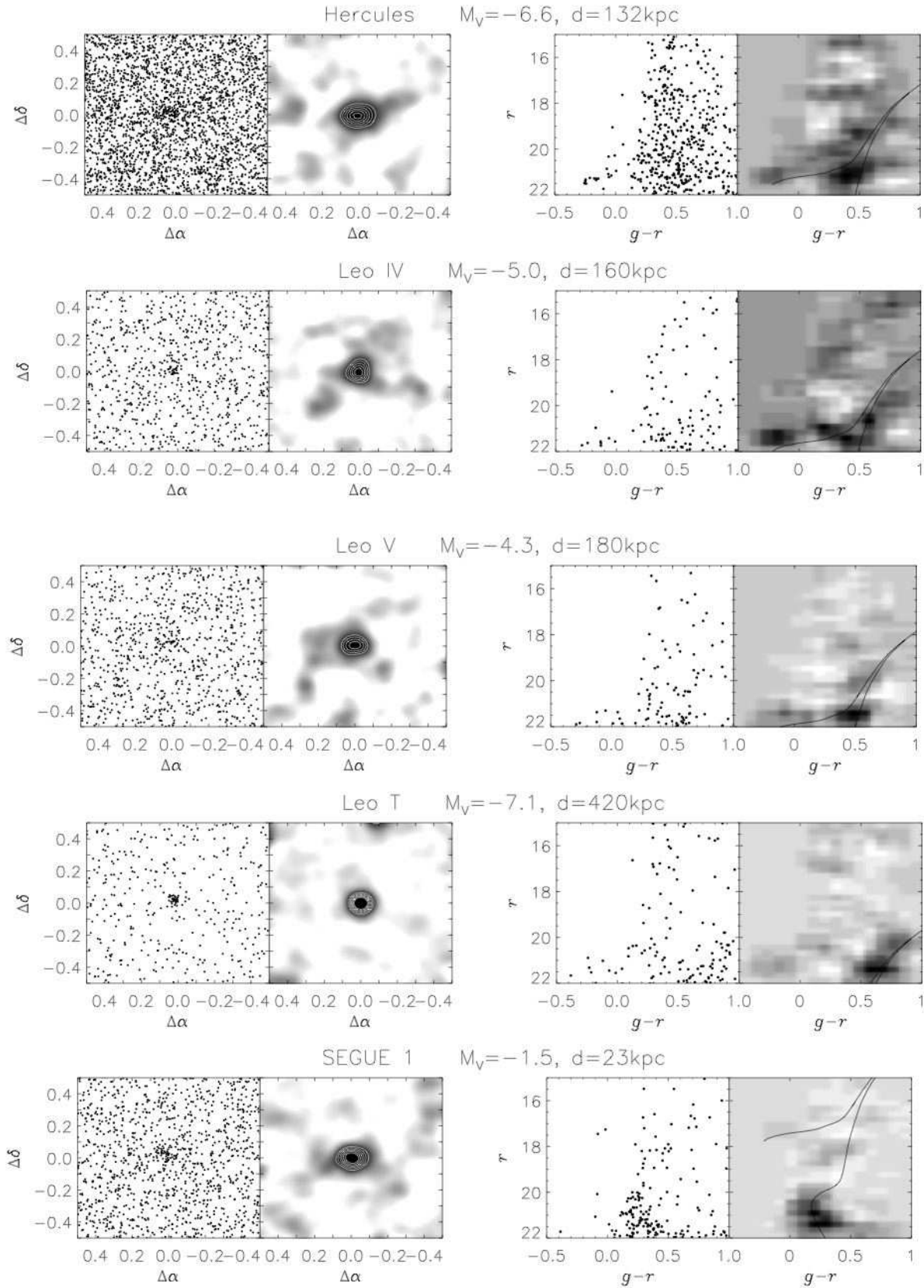


FIG. 7.— Detections of recently discovered MW satellites *cont.*

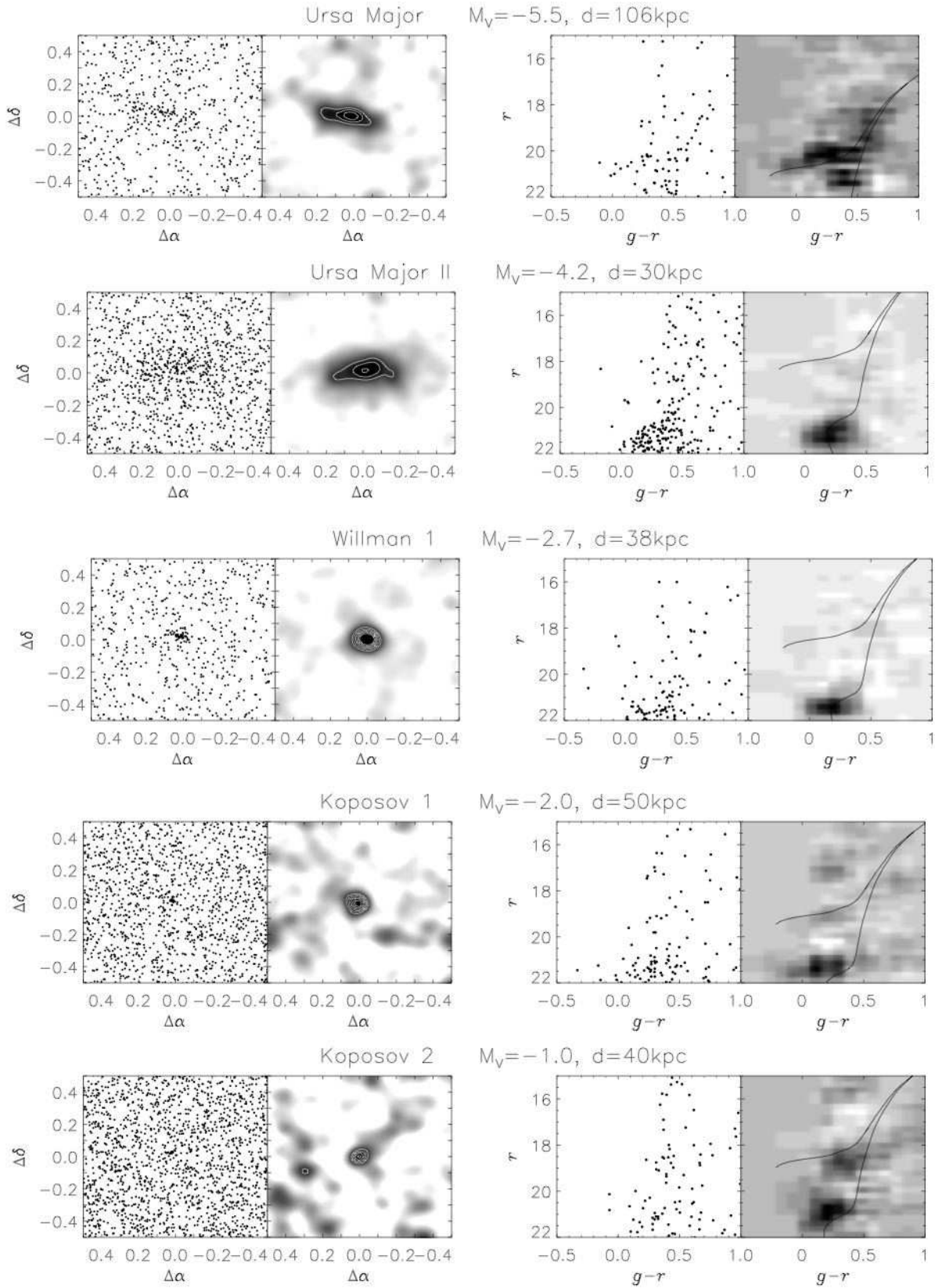


FIG. 8.— Detections of recently discovered MW satellites *cont.*

position in the sky. For example, those at low Galactic latitudes will be harder to detect than those at high lat-

itudes, owing to the greater number of foreground stars. The relative proportions of the thin disk, thick disk, and

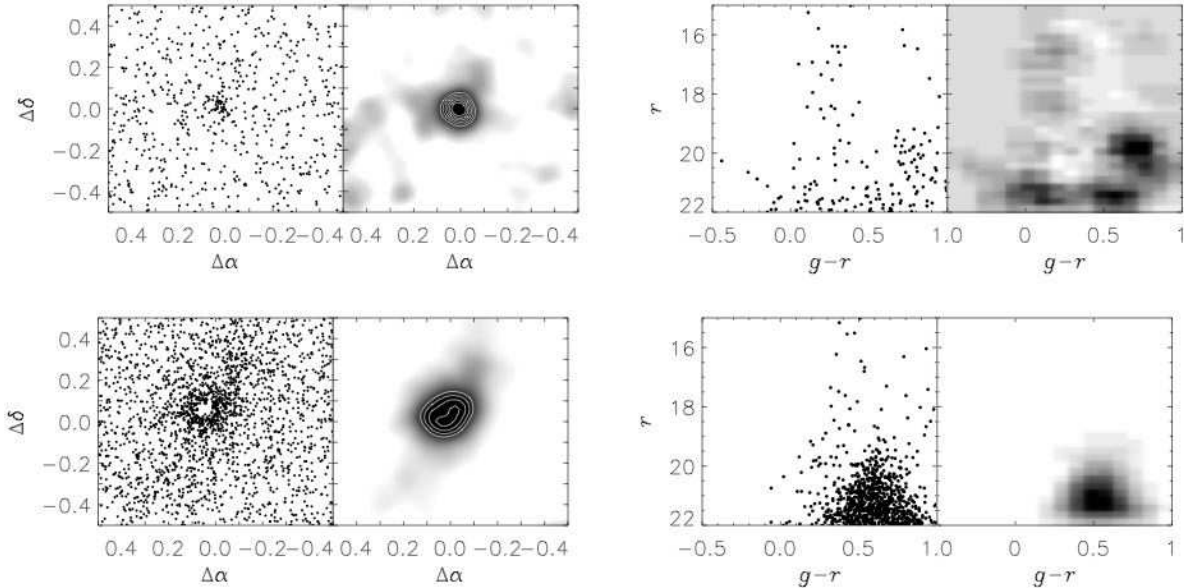


FIG. 9.— Detections of Abell 1413 (top) and NGC 4486 (bottom) as examples of galaxy cluster and background galaxy detections.

stellar halo will also vary with latitude and longitude, changing what fraction of foreground stars will be included in the color-magnitude selection described in §3.

To conduct a controlled experiment to see how Galactic foreground affects detection efficiency over the DR6 footprint, we first select three fiducial latitudes to simulate: the median latitude of the DR6 footprint, and the latitudes above and below which 10% of the survey lies. Figure 11 shows the fraction of sky observed by SDSS DR6 as a function of latitude (dashed line). Weighting this fraction by $\cos b$ gives the relative area on the celestial sphere that each observed latitude occupies (solid grey line), showing that the majority of the DR6 footprint by area is located between $b \approx 45^\circ$ and $b \approx 65^\circ$. The cumulative total (solid black line) allows us to choose the latitudes corresponding to 10, 50 and 90% levels of DR6, namely 31° , 53° and 74° . These are the three values of latitude that we implement in our simulations.

Now that we have chosen what latitudes to simulate, we need to relate these to the stellar foreground density. Figure 12 presents a 2D histogram of latitude and foreground density, considering only stars brighter than $r = 22.0$ and bluer than $g - r = 1.0$. This figure shows a span in foreground levels at each latitude. The solid black line traces the median and our chosen latitudes are marked along the x-axis. For each of our latitudes, we take a slice through the 2D histogram and use this distribution of densities to randomly assign a density for each of our simulated fields. Each artificial star in our simulated fields is assigned photometric parameters from a star in DR6, chosen at random from all stars within $\pm 0.5^\circ$ of the latitude in question. These stars are then randomly distributed in a $3^\circ \times 3^\circ$ field.

5.2. Forging Virtual Dwarfs

To simulate a dSph galaxy CMD, we enlist HST observations of three MW satellites⁶: Carina, Draco, and Ursa

Minor (Holtzman et al. 2006). Figure 13 shows the combined CMD of these objects. We take this M_V and $V - I$ CMD and translate it in color and magnitude loosely to match the Girardi et al. (2004) isochrones g and r . The reasonable agreement between the HST data after approximate transformation and Girardi et al. (2004) isochrones in g and r is sufficient to use the HST data for our simulated objects.

We use these data to create a composite old stellar population catalog of stars brighter than $M_r = 6$ by combining sources from the three HST dwarfs. Carina, Draco, and Ursa Minor each contribute 5,548, 4,487, and 3,296 stars respectively. Each time we simulate a dwarf galaxy of n stars, we select those n stars at random from this composite catalog. The luminosity is calculated from the integrated flux from all stars, and a correction added to account for stars below an absolute magnitude of $M_r = 6$. The cumulative luminosity functions in the right panel of Figure 13 show that typically $\sim 10\%$ of the total flux originates from stars below this cut-off. We then adjust the photometry of the stars to the correct distance modulus and add photometric scatter to reflect increasing measurement uncertainty with fainter magnitudes. We do this by finding the best fit for the 1σ magnitude uncertainty as a function of magnitude for each band in the SDSS data, and adding a normally distributed random realization δ of this value $\sigma(m)$ for the adjusted magnitude, $m_{\text{star}} = m + \delta\sigma(m)$. We then assign random positions based on a Plummer surface brightness profile with a specified physical scale length at a given heliocentric distance.

Figure 14 shows examples of three simulated dSphs. The middle panel shows a system not unlike Boötes II, highlighting the paucity of stars in the objects we are searching for. It is important to note that at these low luminosities, the total luminosity of galaxies with the same number of stars can vary dramatically, with this variation increasing for galaxies with fewer stars. A single RGB star can have a magnitude of $M_r = -3$ which

⁶ <http://astronomy.nmsu.edu/holtz/archival/html/lg.html>

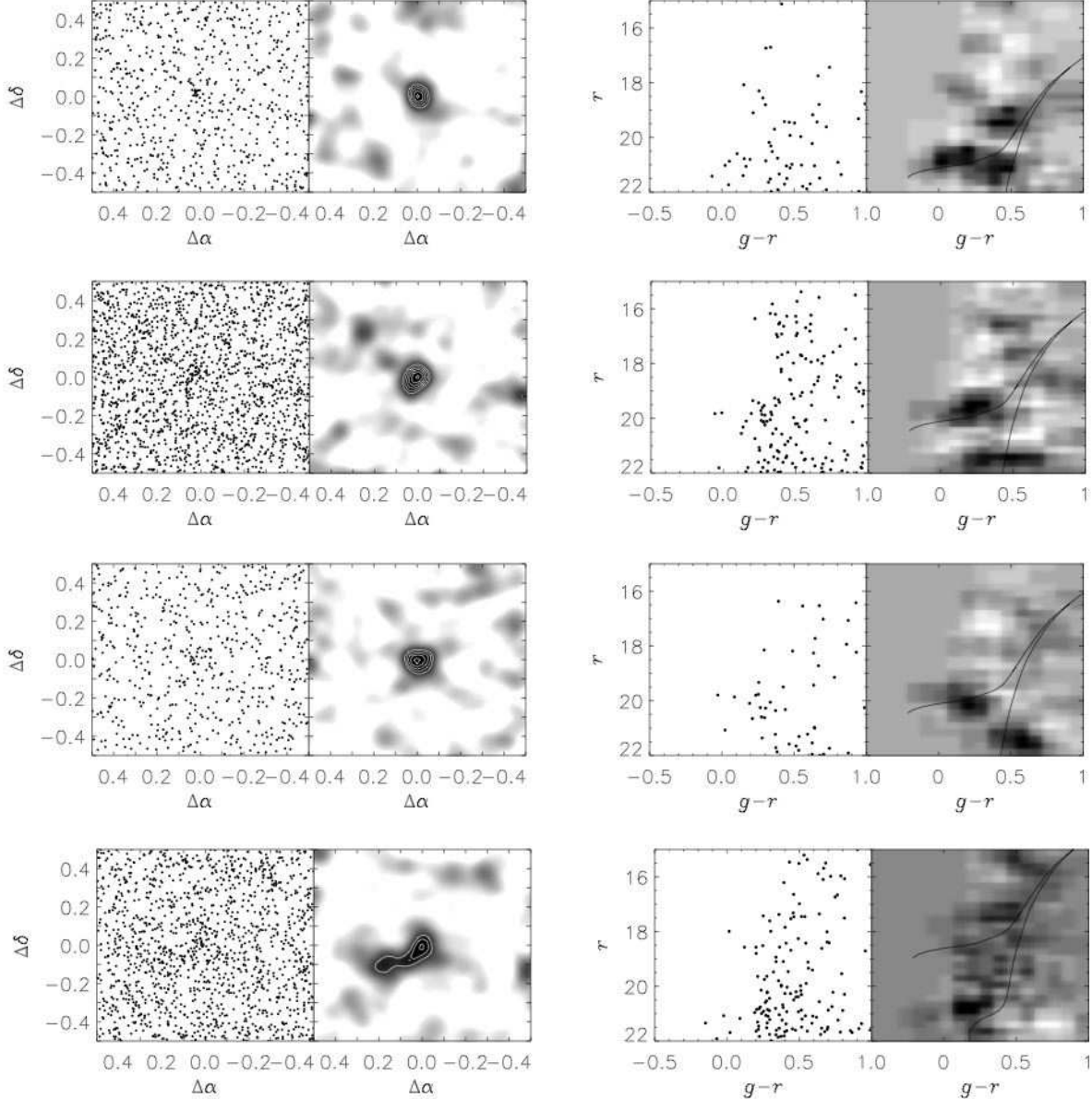


FIG. 10.— The four unknown detections with detection strength equal to or greater than known satellites (except Leo V). From top to bottom: “Canes Venatici W”, “Hercules X”, “Ursa Major Y” and “Virgo Z”. Isochrones show the distance interval at which these overdensities produced the strongest detections.

is well in the regime of the total magnitudes of recently discovered satellites. Each generated galaxy is embedded in a simulated field, and then processed as described in §3.2, §3.3 and §3.4.

5.3. Charting Detection Efficiency

To test the efficiency of our search algorithm as a function of galaxy luminosity, scale-length, distance, and Galactic latitude, we generate a total of 3,825,000 galaxies spanning ranges in Galactic latitude, luminosity, physical size, and distance. We simulate systems at latitudes of 31° , 53° and 73° and with $2^x \times 100$ stars brighter than $M_V = 6$, where x is an integer between 0 and 11 (giving a range of 100 to 204,800 stars). These stellar totals correspond to mean total magnitudes of $M_V = -1.5$, -2.3 , -3.1 , -3.9 , -4.7 , -5.5 , -6.2 , -7.0 , -7.7 , -8.5 , -9.2 and -10.0 . For each of the 36 combinations of

latitude and magnitude, we simulate a large number of galaxies with distances and physical scale-lengths randomly generated with the limits $1.3 < \log d/kpc < 3.0$ and $0.9 < \log r_h/pc < 3.0$. For the brightest and faintest systems we tailor these ranges to avoid redundant iterations; there is little to be gained by simulating a $M_V = -1.5$ system at 200 kpc or a $M_V = -10.0$ system at 20 kpc. Hence, the total number of simulations for each magnitude/latitude combination varies, but is chosen such that there are typically 500 simulations in each $0.1 \log(d) \times 0.1 \log(r_h)$ bin of Figure 15.

6. DISSECTING EFFICIENCY TRENDS

Figure 15 shows the detection efficiency of simulated dwarf galaxies as a function of luminosity, scale-length, and distance at the median SDSS Galactic latitude (53°). Overplotted are each of the Milky Way satellites detected

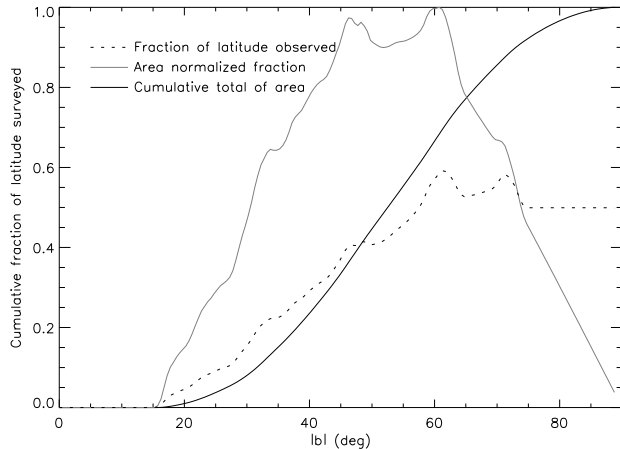


FIG. 11.— The fraction of sky as observed by SDSS DR6 at each latitude. The dotted line shows what fraction of the small circle on the celestial sphere traced by each latitude has been surveyed, and the grey line is this fraction weighted by the cosine of latitude, to give a relative sky area observed at each latitude. The largest area of DR6 observations occur at $b \approx 60^\circ$. The solid black line is the cumulative total of the grey line.

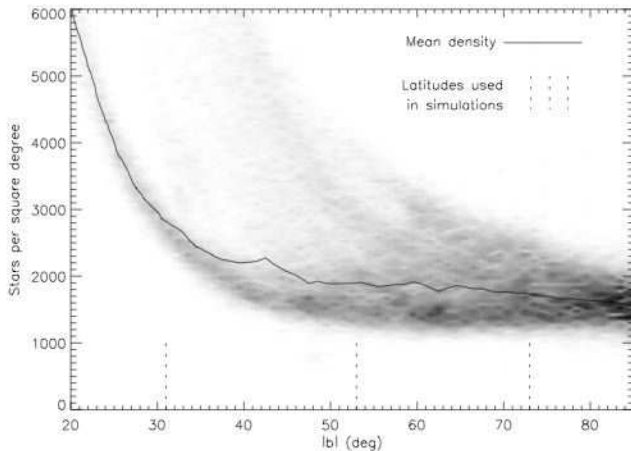


FIG. 12.— Grey-scale plot of the number of sources per square degree satisfying $r < 22.0$ and $g-r < 1.0$ versus absolute Galactic latitude. The black line traces the mean density at each latitude. The three latitudes we choose to simulate are marked along the x-axis.

in SDSS, not including Kopusov 1 and 2. Each panel contains a grey-scale map of the detection efficiency for simulated galaxies of the mean absolute magnitude specified in the panel. Because the total magnitude varies for systems with a constant number of stars, we quote both the mean magnitude and the standard deviation of magnitudes for each panel. White shows regions of 100% efficiency, while black shows 0%. The four contours, moving outwards from 100% efficiency, show the 90%, 84.13%, 50%, and 15.86% levels. The 84.13% and 15.86% levels were chosen to illustrate the $\pm 1\sigma$ in detectability as a function of distance and size.

The greater the number of stars in a simulated galaxy, the less its absolute magnitude will vary between realizations, so the standard deviation in the integrated magnitudes of simulated galaxies contributing to each panel decreases with increasing magnitude. The $M_V = -7.7$

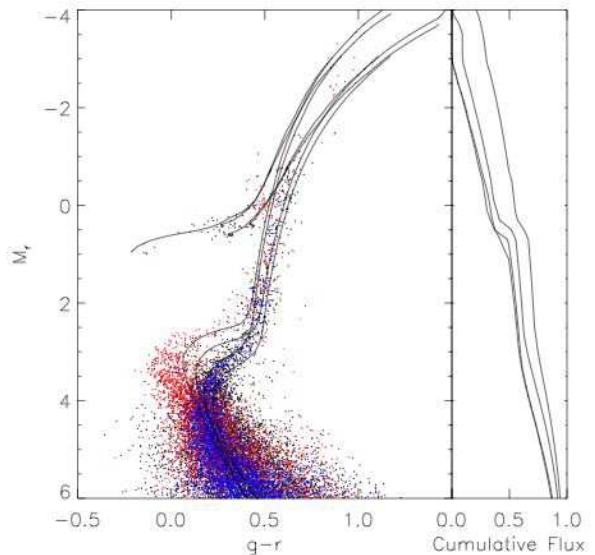


FIG. 13.— HST data of three Milky Way satellite dSphs (Carina, Draco, and Ursa Minor; Holtzman et al. 2006) with SDSS isochrones (Girardi et al. 2004) overlaid. The right panel shows the cumulative luminosity functions for the corresponding isochrones, using the four combinations of $[\text{Fe}/\text{H}] = -2.27, -1.5$ and age = 8, 14 Gyr. Data are corrected for distance and presented in absolute magnitude.

panel which shows a small increase in standard deviation marks a change in the way the galaxies are simulated; we are now simulating systems with more stars than are in our HST catalog so the simulated stars no longer have unique photometry drawn from this catalog. This amplifies the small number effect of single stars on the total magnitude.

Figure 15 illustrates the necessity for a large number of simulations as there are subtle features that would otherwise be unresolved. For example, this figure shows that the detectability of dwarfs is not a step function in distance, but rather slowly falls off at a rate that differs for systems with different total luminosities. This is in contrast to Kopusov et al. (2007a), who found a steep boundary between 100% and 0% efficiency. The gradual fall-off in dwarf detectability with distance will be discussed in more detail in §6.1, but we postpone detailed comparison with Kopusov et al. (2007a) until §7.

The critical factor affecting the detectability of an object with our algorithm is the number of stars brighter than $r = 22.0$ that fall under the $r_h = 4.5'$ Plummer smoothing kernel. In the following sections, we use this to gain physical understanding of the features of Figure 15 and to derive an analytic expression to describe detection efficiency as a function of galaxy magnitude, size, distance, and Galactic latitude. This analytic expression, as well as a routine to interpolate detectability directly from the simulations, will be made publicly available and can be used, for example, to correct the MW satellite luminosity function as previously done by Kopusov et al. (2007a) or make an estimate on the corrected radial distribution of MW satellites. Such endeavours are beyond the scope of this paper, but we use the function to estimate the total number of MW satellites that remain undetected, presented in §8.

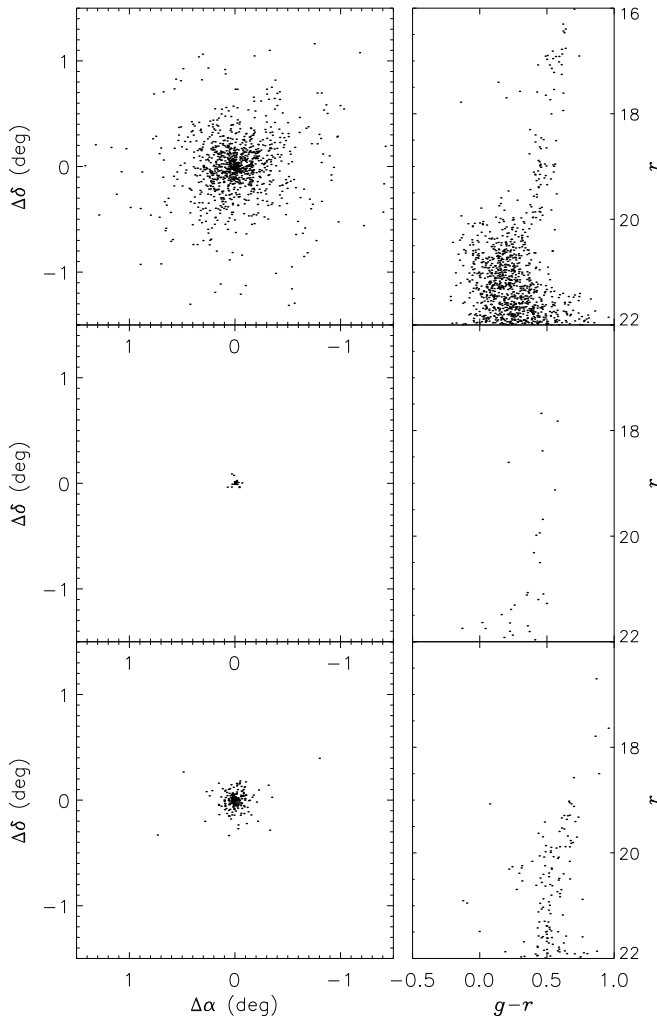


FIG. 14.— Simulated dSph systems.
 Top: $d = 25$ kpc, $r_h = 250$ pc, $M_V = -4.7$.
 Middle: $d = 45$ kpc, $r_h = 40$ pc, $M_V = -2.3$.
 Bottom: $d = 100$ kpc, $r_h = 250$ pc, $M_V = -5.6$.

6.1. Efficiency versus Distance

Figure 15 shows that the detectability of resolved dwarfs around the Milky Way is not a step function in distance. As distance to a dwarf galaxy increases, the number of stars brighter than $r = 22.0$ ($N_{r < 22}$) decreases. In an idealized scenario, the detectability of that dwarf would drop from 100% to 0% at a distance beyond which the number of resolved stars required to produce a detection is larger than $N_{r < 22}$. As we have discussed in previous sections, random variations in the stellar luminosity function can be substantial in the faintest systems, hence $N_{r < 22}$ will be affected by stochastic fluctuations. Moreover, the wide range in foreground densities at a given Galactic latitude (see Figure 12) impacts the detectability of two identical dwarfs. Therefore the transition from 1.0 to 0.0 detection efficiency is not expected to be a step function, but rather described by a Gaussian integral. Koposov et al. (2007a) also modeled the detectability transition with a Gaussian integral, despite finding a steep decline. So detection efficiency as a function of $\log(\text{distance})$, which for brevity we denote ${}_L d$ can

be described as

$$DE({}_L d) = \text{erf} \left(\frac{{}_L \bar{d} - {}_L d}{\sigma_{{}_L d}} \right)$$

where ${}_L d$ is the logarithm of distance, and ${}_L \bar{d}$ and $\sigma_{{}_L d}$ are the mean and standard deviation of $\log(\text{distance})$. The mean corresponds to the distance at which a system would be detected with 50% efficiency. The error function erf is defined as:

$$\text{erf}(x) = \frac{2}{\sqrt{\pi}} \int_0^x e^{-t^2} dt.$$

Examination of Figure 15 shows that $\sigma_{{}_L d}$ (how quickly efficiency transitions from unity to zero) changes depending on luminosity. We would naively expect $\sigma_{{}_L d}$ to continue increasing with decreasing brightness as small number statistics becomes more dominant. Instead it shows a maximum at $M_V \approx -3.9$ before decreasing. This is a result of the stochastic fluctuations and the derivative of the luminosity function; since $N_{r < 22}$ varies for systems with the same total number of stars, the individual distance that each of these systems could be detected at also varies. As the number of stars above the brightness limit is dependent on the LF, the slope of the LF determines how $N_{r < 22}$ changes with distance. Hence $\sigma_{{}_L d}$ is smaller for the faintest objects when the MSTO is required for a detection because the LF is at its steepest at the turnoff.

6.2. Efficiency versus Scale-length

The fraction of a dwarf's stars within our $4.5'$ spatial smoothing kernel decreases with increasing physical scale-length and/or decreasing distance. A system of some luminosity and distance that is detectable when its angular size is $\lesssim 4.5'$ may thus be undetectable if those same stars are spread over a larger angular scale. As the concentration of stars increases we would expect detection efficiency to also increase. However, when the angular size of a dwarf is comparable to the smoothing kernel size, the detectability does not appreciably improve with further decrease in size since the number of stars within the Kernel is not significantly changing. Hence objects of this angular size or smaller will be detected with the same efficiency.

Once the angular size becomes larger than the kernel size, the number of stars within the kernel declines. The relationship between size and detection distance is dependent on the stellar luminosity function of the system. Take for example an object with an angular size larger than the smoothing kernel, detected with 50% efficiency at some distance. To keep the object at 50% efficiency as we continue to increase the physical size, the drop in efficiency can be counteracted by decreasing the object's distance. As this object is moved closer the number of stars above $r = 22.0$ increases at a rate corresponding to the LF. At the distance when the main sequence turn-off (MSTO) becomes brighter than $r = 22.0$ (~ 65 kpc), the rapid increase in the number of stars corresponds to a sudden improvement in detection efficiency, evident in Figure 15 at $\log(d) \approx 1.8$ in the $M_V = -5.5$, -4.7 and -3.9 panels. As with distance, efficiency versus scale-length can be modeled by a Gaussian integral, but with the mean and standard deviations as functions of dis-

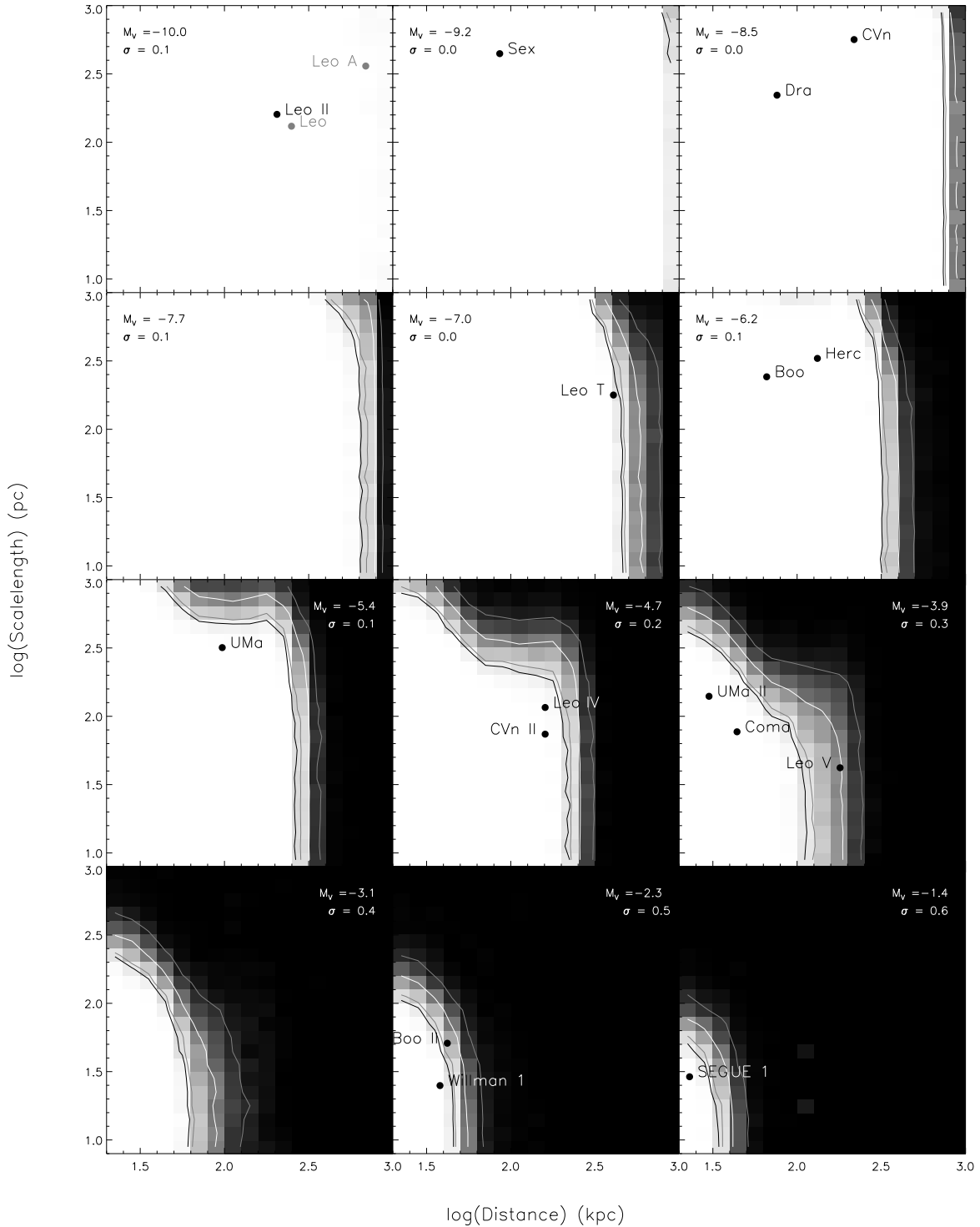


FIG. 15.— Detection Efficiency for specific galaxy parameters. Each panel shows the detection efficiency as functions of distance and scale-length for a particular number of galaxy stars. The average total absolute magnitude for each of these sets of galaxies is shown along with the standard deviation in magnitudes. Contours show the 90%, 84.13%, 50%, and 15.86% levels. Sizes and distances of known MW dSphs are shown in grey in the best matching magnitude panel. Leo and Leo A are shown in grey as they are significantly brighter than $M_V = -10.0$. Values for newly discovered objects plus Draco are taken from Martin et al. (2008) except for Leo V (Belokurov et al. 2008). Values for Leo, Leo II, Leo A, and Sextans taken from Mateo (1998).

tance; so

$$DE(Lr_h) = \text{erf} \left(\frac{L\bar{r}_h(L\bar{d}) - Lr_h}{\sigma_{Lr_h}(Ld)} \right).$$

6.3. Analytically Expressing Detection Efficiency

Combining the previous two results, we can analytically describe detectability with a Gaussian integral over $\log d$ multiplied by another Gaussian integral over $\log r_h$. To introduce magnitude M_V and latitude b , we set the means ($L\bar{d}$, $L\bar{r}_h$) and standard deviations (σ_{Ld} , σ_{Lr_h}) in the integrals to be functions of M_V and b . Therefore the detection efficiency DE can be expressed:

$$DE = \text{erf} \left(\frac{L\bar{d}(M_V, b) - Ld}{\sigma_{Ld}(M_V, b)} \right) \times \text{erf} \left(\frac{L\bar{r}_h(L\bar{d}(M_V, b)) - Lr_h}{\sigma_{Lr_h}(Ld(M_V, b))} \right)$$

The means and standard deviations can be found by fitting Gaussian integrals along the distance and scale-length axes of the panels in Figure 15. The main source of uncertainty in this expression is the galaxy luminosity, which while correlated with the number of stars, can vary by over a magnitude for systems of equal detectability. The function does however give a good statistical approximation from which to estimate the properties of the true Milky Way satellite population. In Figure 16 we compare the $M_V = -3.9$ panel of Figure 15 with the analytical function. There is good agreement between the empirical and analytical detection efficiencies with a 1σ deviation of only $\sim 8.7\%$ across the entire range of parameters. For reference the size of the $4.5'$ smoothing kernel and the distance at which the MSTO becomes resolved are shown in the center panel in red and blue respectively.

The analytical efficiency is compared in Table 3 to the interpolated efficiency from the grids in Figure 15 for real MW dwarfs. For all objects besides Boo II, Leo V, and Leo T, the difference is within $\sim 1\%$. At first inspection it may seem odd that all objects have a very high, almost 100%, efficiency, but given that most of the parameter space probed by our simulations yields either zero or unity efficiency, it is not unexpected that the handful of objects detected in this vast volume are detected with high efficiency.

6.4. Efficiency versus Latitude

Unlike the other parameters which vary a dSph's signal strength, Galactic latitude affects detection efficiency by changing the foreground density, and therefore noise above which we must detect a signal. If latitude plays a significant role in the detectability of dwarfs, then it must be taken into account when making any corrections to the MW satellite census. Figure 17 shows the $M_V \approx -3.9$ panel of Figure 15 ($b = 53^\circ$) with the addition of the 50% detection efficiency (dashed) and 90% detection efficiency (dotted) contours of the $b = 31^\circ$ (orange) and 74° (blue) simulations overplotted. As expected, an object of given size and luminosity will not be detectable as far away at low latitudes as it would be at closer to the Galactic pole. For example, an object with $r_h \approx 30$ pc and $M_V \approx -3.9$ at $b = 74^\circ$ can be detected with 90% efficiency as far as ~ 120 kpc, while the same object at $b = 31^\circ$ has a 90% efficiency at ~ 95 kpc.

To anticipate the effect that varying Galactic foreground will affect future dwarf searches in data that goes

TABLE 3
COMPARISON OF INTERPOLATED AND
ANALYTICAL DETECTION
EFFICIENCIES

Object	Interp.	Analyt.	Diff.
Boo	99.84	99.98	-0.14
Boo II	90.39	95.96	-5.57
CVn	100.0	100.0	0.0
CVn II	98.26	99.07	-0.81
Com	99.71	100.0	-0.29
Dra	100.0	100.0	0.0
Her	99.82	99.83	-0.01
Leo	100.0	100.0	0.0
Leo II	100.0	100.0	0.0
Leo A	100.0	100.0	0.0
Leo IV	98.65	99.77	-1.12
Leo V	83.56	91.27	-7.71
Leo T	93.41	99.38	-5.97
Segue 1	100.0	100.0	0.0
Sex	100.0	100.0	0.0
UMa	99.97	99.86	0.11
UMa II	100.0	99.96	0.04
Will 1	98.56	99.30	-0.74

closer to the Galactic plane than SDSS, we also repeat the simulation of $M_V \approx -3.9$ galaxies at a foreground density of 10,000 stars per square degree, approximating a latitude of $\sim 15^\circ$. The 50% and 90% detection efficiency contours (red) for these simulations are also shown on Figure 17. This further reduces the 90% detection distance of our example object to ~ 80 kpc but demonstrates that future surveys should still detect dwarfs at relatively low Galactic latitudes, barring extinction effects.

To check that latitude has the same lack of effect over different magnitudes, we calculate the 50%, 90%, and 99% detection efficiency distance for a $r_h = 100$ pc object over the magnitude range $-1.5 < M_V < -7.0$ at $b = 31^\circ$, 53° , and 71° (Figure 18, note that in this figure the distance scale is linear). The 53° and 71° curves are indistinguishable and the $b = 31^\circ$ curve is typically less than 20 kpc lower. This demonstrates that over the DR6 footprint, latitude does not play an important role on average in the detectability of objects. However, if we are unlucky, then individual objects could by chance lie in directions of unusually high foreground counts.

6.5. Comparing R_{99} , R_{90} and R_{50}

We use the analytical expression derived in §6.4 to estimate the distance at which each of the Milky Way dwarfs would be detected with 50% efficiency, R_{50} (Figure 19, grey dots). Because R_{50} depends on half-light radius, as well as luminosity, we also for reference show R_{50} for objects with $r_h = 250$ pc (red) and $r_h = 50$ pc (blue). These lines show that the detectability of the lowest luminosity dwarfs is severely reduced for large scale sizes. Objects with Segue 1, Boötes II, or Willman 1-like luminosities would not have been detectable with scale sizes of 100 pc or larger, even at very nearby distances. This size bias is important to bear in mind, particularly given that the three M31 satellites discovered by McConnachie et al. (2008) that highlight regions of dwarf galaxy parameter space that have not previously been observationally seen.

Assuming the size-luminosity distribution of known

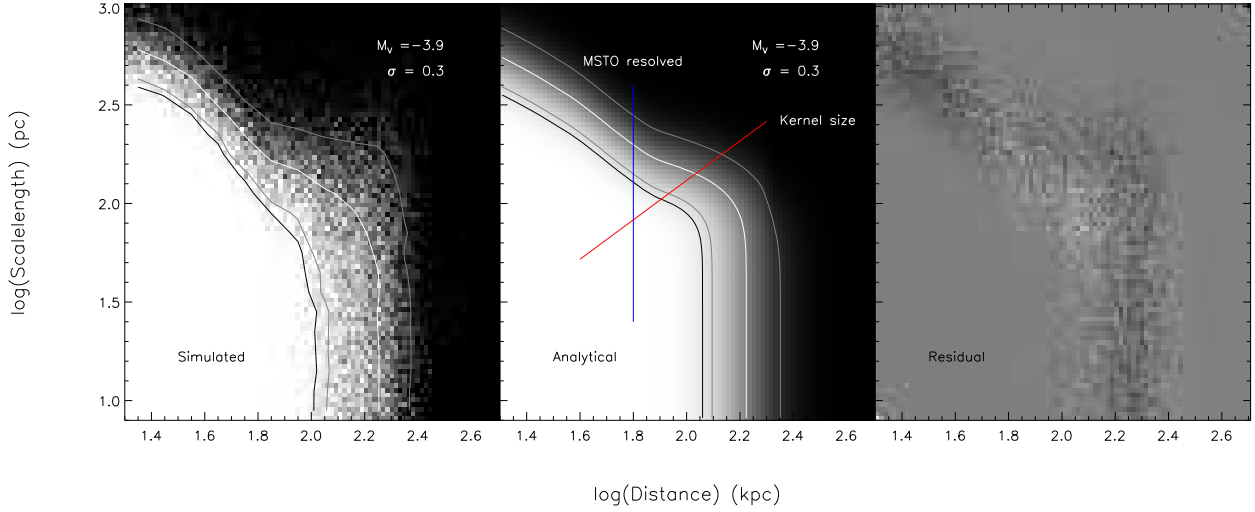


FIG. 16.— *Left*: $M_V = -3.9$ panel of Figure 15 binned to higher resolution. *Center*: Same as left panel but using the analytical expression to estimate detection efficiency. *Right*: Residual of the model-analytical efficiency.

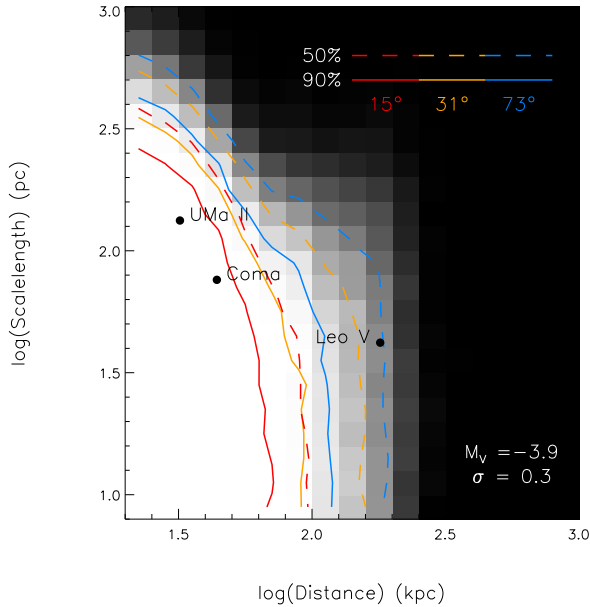


FIG. 17.— The same as the $M_V = -3.9$ panel of Figure 15, but showing the 50% and 90% contours of the simulations at $b = 74^\circ$ (blue), 31° (orange), and $\sim 15^\circ$ (red).

satellites is representative of all satellites we can ignore size and approximate R_{50} as a function of M_V by linear fit to the R_{50} of actual dwarfs:

$$\log R_{50} = -0.187M_V + 1.420.$$

For comparison, the Koposov et al. (2007a) equivalent of R_{50} is shown in Figure 19 (dotted line) obtained from Table 3 in their paper, and discussed further in §7. For reference, the actual distances to the MW dwarfs are shown as black dots.

A more useful quantity might be $R_{complete}$, the maximum distance at which objects can be detected. Although we choose to use “complete” to refer to 90% de-

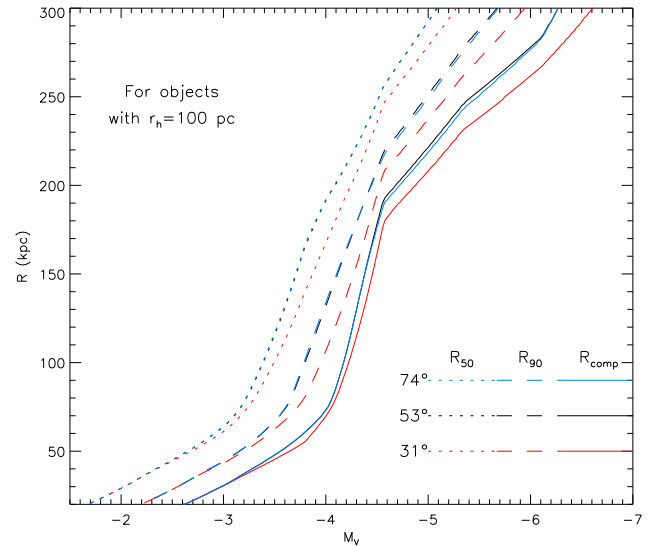


FIG. 18.— 50%, 90%, and 99% completeness distances for a $r_h = 100$ pc object as a function of magnitude at three Galactic latitudes: 31° , 53° and 71° . The 53° and 71° curves are virtually indistinguishable showing that latitude does not significantly impact satellite detection over latitude ranges of DR6.

tectability, complete could be defined as, say 90% or 99% efficiency. This can also be approximated by a linear fit to the results for the actual MW dwarfs:

$$\log R_{90} = -0.204M_V + 1.164$$

or

$$\log R_{99} = -0.217M_V + 1.005.$$

These relationships again assume that the known satellites are typical of the MW satellite population as a whole, i.e. objects with luminosities comparable to Segue 1 are similar in size to Segue 1 and not significantly larger.

Returning to Figure 18 we see the distance range over which detectability changes from 99% to 50%. R_{90} is

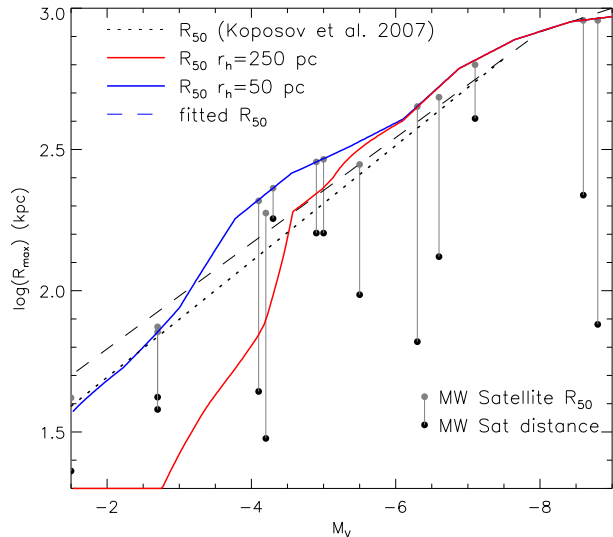


FIG. 19.— Comparison of the 50% detection distance as a function of magnitude for K07 (dotted) and for our analytical efficiency using $r_h = 250$ pc (red) and $r_h = 50$ pc (blue). MW dwarfs are shown as filled circles.

typically ~ 20 kpc closer than R_{50} , and R_{99} is ~ 20 kpc closer still. From this figure we can also see that objects brighter than $M_V \approx -6.5$ mag ($M_V \approx -5.9$ mag) are detected with 99% (90%) efficiency out to 300 kpc. We can infer from this that all dwarfs within the MW virial radius brighter than $M_V \approx -6.5$ mag are known, and any satellites still undetected are likely to be reminiscent of objects like Coma Berenices, Boötes II or Segue 1 at distances greater than ~ 40 kpc. An ultra-faint satellite such as Segue 1 can only be detected with 50% efficiency out to ~ 40 kpc; there may be many more such objects beyond this distance.

The code for interpolating detection efficiency from our simulations as well as the analytical function will be made available for download at the Astronomical Journal website. Interpolation will give more accurate results, but the analytical function will provide flexibility for customization to suit individual needs and implementation of any future improvements.

6.6. Caveats

An underlying assumption of our simulations is that the DR6 point source catalog is uniformly 100% complete to $r = 22.0$. This assumption may result in optimistic detection efficiency estimates for the faintest and furthest systems. These faintest and more distant systems would also be subject to the human element; a real object may be detected by the algorithm but on visual inspection be disregarded as background galaxy cluster or other contaminant. Finally, sources in our simulated dSphs are distributed circularly symmetrically. Martin et al. (2008) find that the ultra-faint satellites are in fact quite elliptical, which due to our circular Plummer smoothing kernel, possibly results in overestimated efficiencies for objects like Hercules, UMa and UMa II with ellipticities of 0.68, 0.80 and 0.63 respectively.

7. COMPARISON WITH KOPOSOV ET AL. (2008)

Besides Willman et al. (2002) from which this work follows, two other surveys have recently uniformly searched SDSS for MW satellites, namely Liu et al. (2008) and Koposov et al. (2007a). Liu et al. (2008) conducted a straightforward search and presented five satellite candidates. Koposov et al. (2007a) present a study comparable to this work, and follows from the “Field of Streams” (Belokurov et al. 2006a) that led to the discoveries of nine of the new Milky Way satellites. Here we compare our work in detail with Koposov et al. (2007a) and summarize the main differences in Table 4.

The aim of Koposov et al. (2007a) was to present a luminosity function of the MW satellites corrected for luminosity bias. Their analysis discovered two new extremely faint globular clusters, Koposov 1 and 2 (Koposov et al. 2007b). In principle, our analysis is quite similar to Koposov et al. (2007a), henceforth K07, in that they apply a color cut, smooth the stellar counts and look for statistically significant overdensities. There are several distinctions however that we detail below.

K07 employed a $g - r < 1.2$ color cut to remove a substantial fraction of MW foreground stars and a $r < 22.5$ cut to limit the influence of background galaxies and increasing uncertainties/incompleteness. Our color-magnitude cuts are tailored to old stellar populations at 16 different distances which serve to eliminate more foreground stars than the looser K07 cut. The looser K07 color cut leaves enough stars that a complicated set of detection thresholds is unnecessary, whereas we must consider the effects of non-Gaussianity in low densities (see §3.4). K07 deals with background galaxy clusters, a major source of contaminant overdensities, by producing a galaxy clustering significance in the same manner as the stellar clustering; anywhere that a stellar overdensity occurs without a corresponding galaxy overdensity is much more likely to be a true stellar overdensity. Our algorithm only includes stars as faint as $r = 22.0$ and as such we have fewer galaxy cluster contaminant detections.

The most substantial difference between our work and K07 is how we derive the detection limits of our algorithms. Like our work, K07 simulated artificial galaxies to explore the detection efficiency as a function of size, distance and luminosity. K07 simulated 8,000 galaxies over a similar range of parameters as our study, but with only ~ 8 objects per $0.3 \log(d) \times 0.3 \log(r_h) \times 0.8$ mag bin. There is considerable noise evident in the detection limits (their Figure 6), and all of the new satellites appear to lie on the edge of detectability. K07 observed a steep, but finite, transition from unity to zero detection efficiency which they attributed to the large range of distances that fall within each size-luminosity bin. However, as discussed in our §5.2, a large number of simulated galaxies are essential for each permutation of dwarf galaxy parameters to effectively map their detectability. Our high resolution detection maps (~ 500 objects per $0.1 \log(d) \times 0.1 \log(r_h) \times 0.8$ mag bin, $\times 3$ latitudes) show that the detectability of a dwarf drops off slowly with size and distance, and that only Leo T, Leo IV, Leo V, Boo II and Willman 1 lie close to the edge of detectability. The difference between 90% and 10% efficiency typically occurs over 0.2 dex in distance (kpc) and 0.3 dex in size (pc; see Figure 15).

Both the K07 and our detection limit calculations suf-

fer from the implicit assumptions that the SDSS point source catalog is complete to the photometry limit and that dwarfs are circularly symmetric. These two assumptions yield detection limits that may be optimistic. The K07 study includes stars to a limiting magnitude of $r = 22.5$ mag, a half magnitude fainter than our limit of $r = 22.0$ mag. We thus expect that the completeness assumption may impact their calculated limits more than ours.

To directly compare the effectiveness of both algorithms we return to Figure 19, showing the distance at which an object is detected with 50% efficiency, R_{50} as a function of magnitude. The dashed line shows the K07 R_{50} which was determined by fitting a limiting magnitude and surface brightness to the seven distance panels in their Figure 10. The dots show our R_{50} derived from the analytical efficiency function for each of the MW dwarfs in DR6, while the red and blue curves show R_{50} calculated for objects of $r_h = 250$ pc and $r_h = 50$ pc respectively.

Although this comparison roughly shows that we have comparable limits, our calculated detection efficiencies of each dwarf are all greater than 90% while Table 2 of K07 lists efficiencies as low as 47% (neglecting Boo II). While Boötes II is not detected with the standard algorithm of K07, it is a comparatively strong detection in our algorithm. We note that the tabulated K07 efficiencies for the known MW dwarfs appear inconsistent with their fitted R_{50} , which places some dwarfs much closer than R_{50} than their actual efficiencies would indicate. The increased dwarf detectability of our survey is owing to a combination of different techniques and our less stringent detection threshold. We set our thresholds to strictly eliminate truly random false positives expected while still yielding new candidates, and hence have ~ 30 unknown detections above our thresholds. Although upon visual inspection of their CMDs many of these detections appear unlikely to be new dSph satellites, they may also be tidal debris or distant galaxy clusters. However, K07 set their detection thresholds just loose enough to retain all known objects; UMa is their weakest detection and there are only three unknown detections above this threshold.

8. THE STILL MISSING SATELLITES

A substantial driving force of this work is the Missing Satellite problem, which the discovery of so many new objects in the space of three years has shown is far from observationally exhausted. There are still large regions of parameter space where objects are undetectable, so there can easily exist more objects within the DR6 coverage that remain hidden. Future surveys such as the Stromlo Missing Satellites (SMS) Survey and Pan-STARRS may be able to detect some of these objects, and we can use our model of detectability to estimate how many there may be.

We use a simplified version of the approach used in Tollerud et al. (2008). We first assume that the radial distribution of dwarf galaxies matches that of all well-resolved subhaloes of the Via Lactea simulation (Diemand et al. 2007). Tollerud et al. (2008) discusses this assumption in detail; we realize this may not reflect the true MW dwarf distribution, but our qualitative results are fairly robust to the assumed profile. For each satellite detected in DR6, we then determine R_{90}

(or R_{99}), the maximum distance to which a satellite of similar properties would be detected with 90% (99%) efficiency. For each value of R_{90} (R_{99}), we determine from the Via Lactea subhalo radial profile what fraction of satellites should be within this distance, and weight each satellite accordingly.

Using all dark matter subhaloes with more than 1000 particles within $r_{vir} = 289$ kpc, and adopting a MW virial radius of 258 kpc (Klypin et al. 2002), we estimate ~ 13 (~ 24) satellites within the MW virial radius in the DR6 footprint. Twelve of these would be the known objects Boötes, Draco, Canes Venatici I and II, Coma Berenices, Leo I, Leo II, Leo IV, Leo V, Hercules, Ursa Major, and Ursa Major II, leaving one (12) possible missing satellite(s). From our simulations, objects brighter than $M_V = -6.5$ mag are detectable with $> 99\%$ efficiency out to the virial radius, so we would expect that a relatively small number of the faintest systems are missing. These missing satellites may be amongst our candidates, or be Coma Berenices like or fainter objects in the outer halo. Whether or not future searches reveal such objects may validate the assumed radial distribution. If we assume an isotropic sky distribution of satellites, ~ 13 (~ 24) objects within DR6 equates to ~ 52 (~ 96) across the whole sky.

If we include the ambiguous objects Segue 1, Willman 1, and Boötes II 1 in the calculation, then the R_{90} (R_{99}) DR6 estimate would be ~ 56 (~ 85) satellites only 15 of which are known, or ~ 224 (~ 340) across the sky. The ambiguity of Segue 1, Willman 1, and Boötes II has considerable effect on the extrapolated MW census, underscoring the need for an understanding of these extremely faint systems.

These estimates assume that the sizes and luminosities of the known satellites in DR6 are representative of the the MW satellite population as a whole. Based on our detection limits we cannot make any statements regarding extremely diffuse, low luminosity systems that are undetectable by SDSS. The results also depend on the radial distribution assumed. If we instead assume that the Milky Way's dwarf population follows the radial distribution of the MW dSphs known prior to 2004, then our R_{90} inferred total number of dwarfs (with size-luminosities similar to known) within DR6 is 12, or 25 including Segue 1, Willman 1 and Boötes II. This implies that all or most satellites within DR6 would be known.

Tollerud et al. (2008) use the detection limits of Koposov et al. (2007a) to similarly estimate the true number of satellites within DR5 for a number of scenarios. The most comparable scenario to our assumptions (a limiting distance of 300 kpc, including all satellites except Segue 1 which is not in DR5) gives a result of 322_{-75}^{+144} satellites, consistent with our results of 232 for R_{90} and 344 for R_{99} .

9. ALLOWING A LITTLE LATITUDE

Substantial effort has gone into the observation and interpretation of the spatial distribution of the satellites of disk galaxies, in particular that of the Milky Way satellites. However, there is neither agreement on whether the Milky Way satellites have a truly anisotropic spatial distribution, nor whether we expect them to. Pre-SDSS, Kroupa et al. (2005) found that the distribution of known MW satellites could be described by a disk of

TABLE 4
SUMMARY OF COMPARISON WITH KOPOSOV ET AL. (2008).

	This work	Koposov et al. (2007)
Survey Area	DR6 - 9,500 sq deg	DR5 - 8,000 sq deg
Source cuts	Isochrone template at 16 dist intervals	$g - r < 1.2$ and $r < 22.5$
Smoothing kernel	4.5' Plummer profile	$\sigma = 2', 4', 8' - \sigma = 60'$ Gaussians
Threshold	Multiple, function of foreground density	Fixed, considers background galaxies
Modeled detection limits	HST obs of 3 MW dSphs	M92 locus
Number of Simulations	3,825,000	8,000 for general simulation + 1,000 each for known dwarfs within DR5
Efficiency map bin size ($\log(r_h) \times \log(d) \times M_V$)	$0.1 \times 0.1 \times 0.8$	$0.3 \times 0.3 \times 0.8$
Simulation density (n per $0.3 \times 0.3 \times 0.8$ bin)	~ 4500 ($\times 3$ latitudes)	~ 8

finite width, aligned almost perpendicularly to the MW disk. This was in agreement with the “Holmberg” effect (Holmberg 1969), that the closest satellites to a host galaxy were observed to be preferentially aligned with the minor axis of the host. This disk-like distribution seemed incompatible with Λ CDM, but Kang et al. (2005) reasoned that if satellites follow the distribution of the host dark matter profile rather than that of the substructure then the dozen observed MW satellites could statistically lie in a disk-like structure, although the orientation of this disk is arbitrary. Piatek et al. (2007) used proper motions derived from HST observations to show that this “Great Disk of Milky Way Satellites” was not a persistent structure; the orbits of the dwarfs would not contain them within this disk. Metz et al. (2008) refute this conclusion, finding instead that the orbital poles of most MW satellites place them in a rotationally supported disk-of-satellites. Studies on the satellites of other galaxies from SDSS also yield conflicting results. Bailin et al. (2007) affirm the Holmberg effect while Brainerd (2005) find that satellites lie preferentially along the major, not minor, axis of the host. Zentner et al. (2005) re-examine the problem from a theoretical point of view, stating that DM substructure is not completely isotropic and that the MW satellite distribution can, albeit with a very low probability, be drawn from a DM subhalo distribution.

Within the standard Λ CDM structure formation scenario, satellite galaxies without dark matter could be formed in gas-rich tidal tails during vigorous early galaxy–galaxy interactions (Okazaki & Taniguchi 2000). Families of such tidal dwarfs would have correlated orbital angular momenta and may appear as disk like arrangements about some hosts. This would support the apparent disk-of-satellites (Kroupa et al. 2005; Metz et al. 2007) and its correlated orbital angular momenta (Metz et al. 2008). It is therefore crucial to further constrain the spatial and orbital angular momentum properties of the satellites to reveal their true nature which is intimately related to the formation of the MW.

A caveat of past studies of the MW dwarf distribution is that the sky had not been uniformly searched for satellites and the effect of Galactic latitude on the observability of dwarfs had not been thoroughly quantified. In their detailed study, Kleyna et al. (1997) showed that latitude strongly affected the detectability of Milky Way satellites with their technique. Our uniform study of SDSS DR6 takes their approach a step further and provides a detailed quantitative description of dwarf detectabil-

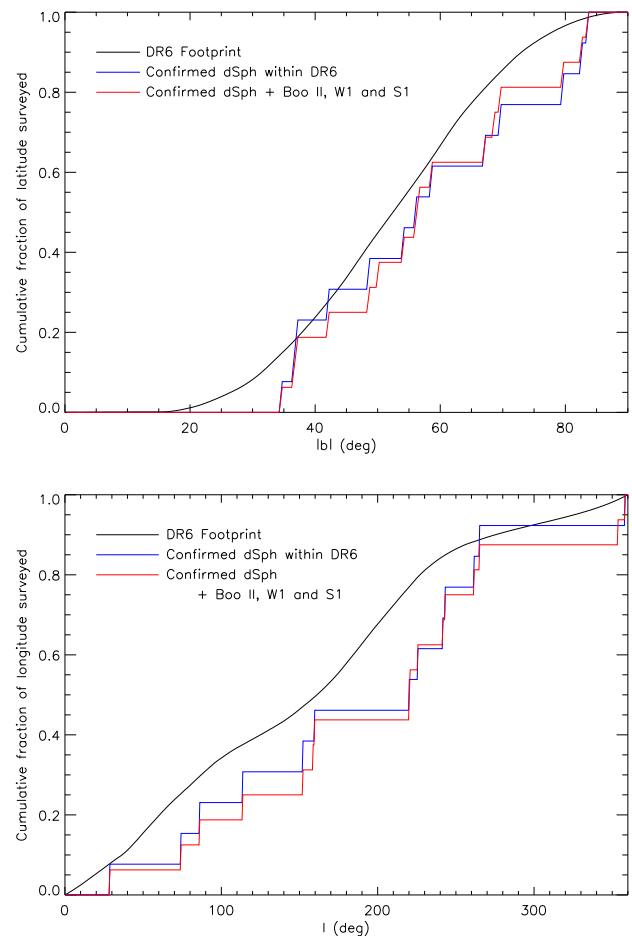


FIG. 20.— *Top*: Cumulative histogram of the Galactic latitude of the DR6 footprint weighted by area (black). Blue shows the cumulative histogram of the latitudes of confirmed dSphs within DR6 and the MW virial radius (Boo, Dra, CVn, CVn II, ComBer, Leo I, Leo II, Leo IV, Her, UMa, and UMa II). Red shows the same but including Boo II, Willman 1, and Segue 1. *Bottom*: Same as top panel, but for Galactic longitude.

ity over the footprint of our survey. We established in §6.4 that the average detectability of the known satellites does not significantly vary over the DR6 footprint. We can thus compare the latitude and longitude distribution of the Milky Way satellites within the DR6 footprint with that expected if they are randomly distributed. We perform a Kolmogorov-Smirnoff test to determine whether

the satellites detected in DR6 show statistically significant spatial anisotropy. Figure 20 shows the cumulative distribution (black lines) of latitude (top) and longitude (bottom) by area of the DR6 footprint. Overplotted on both panels are the cumulative distributions of MW satellites, both ignoring the ambiguous objects Boo II, Willman 1 and Segue 1 (blue) and including them (red). A KS test on these distributions with the entire DR6 area yields a probability of isotropic distribution of 0.16 over longitude and 0.72 over latitude, or 0.06 and 0.79 if we include Segue 1, Willman 1, and Boötes II. We also randomly pick 12 (or 15) points from DR6 coverage, weighted by area, and repeat the KS test 1,000 times. The mean resulting probabilities of isotropic distributions are 0.45 ± 0.29 over longitude and 0.62 ± 0.27 over latitude, or 0.34 ± 0.28 and 0.55 ± 0.28 with Segue 1, Willman 1, and Boötes II. Hence, a conclusive result on the isotropy of the MW satellites awaits further data as our test shows that considering DR6 alone either scenario is plausible.

10. TOWARDS SKYMAPPER

SDSS Data Release 6 covers $\sim \pi$ steradians of Northern sky near the North Galactic Pole, and at least nine new dSph companions have been found in this area. The new ANU SkyMapper telescope will survey the entire southern sky to a similar depth as SDSS over the next five years, so we can naively expect to find around twenty-five new Milky Way satellites. With a detailed, systematic search covering around three quarters of the sky, we will for the first time be able to conclusively compare the MW satellite galaxy population with theoretical predictions. The apparent anisotropy of the satellites will be conclusively confirmed or ruled out and we will continue to discover the most dark matter dominated stellar systems nature produced.

Designed as a replacement for the Great Melbourne Telescope that was destroyed by the Canberra bush fires in January 2003, SkyMapper is a new wide-field automated survey telescope currently being built at Siding Spring Observatory, NSW. It will feature a 1.33m primary mirror and a 0.69m secondary with an effective aperture of 1.13m and a 5.7 square degree field of view. The imager consists of a 4×8 mosaic of 2048×4096 pixel CCDs (Keller et al. 2007). SkyMapper’s primary purpose is the Southern Sky Survey which will be used to study objects from Trans-Neptunian Objects to high redshift quasars. It’s five year mission: to survey the entire 2π steradians of the southern sky at multiple epochs.

Keller et al. (2007) states an average seeing at Siding Spring of ~ 1.5 arcsec as derived from observing logs of the Anglo-Australian Telescope (AAT), on par with the median 1.4 arcsec seeing of the SDSS site (Adelman-McCarthy et al. 2007). The sky will be observed at six epochs, and at completion 90% of the sky will be observed at least five times, and 100% observed at least three times. The expected survey depth ($S/N = 5$, $t=110s$ per epoch) is given in Table 5. Also included are the corresponding magnitude limits from SDSS (Adelman-McCarthy et al. 2007). The survey aims to provide astrometry to better than 50 mas, as compared with 100 mas for SDSS. Further information

TABLE 5
PHOTOMETRIC DEPTHS OF SKYMAPPER^a AND SDSS^b

Filter	SM 1 epoch	SM 6 epoch	SDSS
<i>u</i>	21.5	22.9	22.0
<i>v</i>	21.3	22.7	-
<i>g</i>	21.9	22.9	22.2
<i>r</i>	21.6	22.6	22.2
<i>i</i>	21.0	22.0	21.3
<i>z</i>	20.6	21.5	20.5

^a Expected, Keller et al. (2007)

^b Adelman-McCarthy et al. (2007)

is available at the SkyMapper website⁷.

11. CONCLUSION

The dwarf galaxy satellites of the Milky Way provide excellent opportunities to further our understanding of galaxy formation and near-field cosmology. They can be resolved into individual stars allowing detailed studies of their structure, kinematics and composition. They have also been cause for concern regarding their interpretation as the luminous components of dark matter substructure; it has been argued that the number and spatial distribution of these satellites are inconsistent with Λ CDM structure formation scenarios. The commencement of the Sloan Digital Sky Survey triggered a cascade of discoveries, with fourteen new satellites discovered. The limited spatial coverage and photometric depth of SDSS suggests that many, if not most, MW satellites are still yet to be discovered. The coming years are likely to bring the MW satellite census towards completeness as new survey telescopes such as SkyMapper, Pan-STARRS and LSST come online.

We present here the method used to search the Sloan Digital Sky Survey Data Release 6 for ultra-faint Milky Way satellite galaxies. By screening for stars consistent with an old population at a fixed distance, we enhance the signal of a dSph over the Milky Way foreground. Smoothing with a kernel corresponding to the expected surface density profile further elevates the dSph above the foreground, and our comprehensive thresholds account for varying stellar density and more diffuse objects.

Applying our algorithm to SDSS DR6, we recover the “classical” and recently discovered dSphs, as well as 17 globular clusters and two open clusters. We also have 30 unidentified detections, some of which may be new satellites. The discovery of Leo V demonstrates the difficulty in following-up dwarf candidates; while we detect Leo V, there are several unknown detections of greater significance that may prove to be something. However observing these weakest candidates is a rather hit and miss affair, as pointed out by Belokurov et al. (2008).

To compare the known dwarf galaxy population of the Milky Way with predictions, its essential to have a very well-defined dwarf selection function. To do this, we thoroughly model the detection efficiency of systems covering a wide range in parameter space by simulating more than 3,000,000 galaxies. We fit various functions to the resulting detection efficiency contours to semi-analytically describe efficiency as a function of magni-

⁷ <http://www.mso.anu.edu.au/SkyMapper>

tude, size, distance and Galactic latitude. Using the results of our detailed investigation of dwarf detectability, we show that:

- Assuming a Via Lactea subhalo radial distribution and that $R_{complete} = R_{90}$, there should be ~ 13 satellites with DR6, 12 of which are known. If we include Segue 1, Willman 1, and Boötes II in this calculation, this estimate jumps to ~ 56 , only 15 of which are known.
- Dwarf detectability shows a smooth transition from 100% to 0% over size and distance. For example, the distance at which a CVn II-like object is detected with 90% efficiency is 200 kpc, compared to 316 kpc for 10% efficiency.
- Galactic latitude does not significantly impact the detection of satellites over the DR6 footprint, and surveys of similar quality should still detect dwarfs as low as $b \approx 15^\circ$. All of the satellites discovered in SDSS would have been detected at any latitude.
- The census of MW satellites brighter than $M_V = -6.5$ should be complete out to 300 kpc, and all objects brighter than $M_V = -5$ would be detected with at least 50% efficiency out to this distance.
- Given the present data, the spatial anisotropy of the MW satellites within DR6 cannot be confirmed or ruled out.

We provide several different parameterizations of our detection limits to facilitate comparisons between the known Milky Way dwarf galaxy population and predictions. We provide software that returns the detection efficiency of a dwarf galaxy as a function of its luminosity, scale size, distance, and latitude. There are two different codes provided for this; one is based on an analytic description of our detection limits and the other provides a

direct interpolation from our 3,825,000 simulated galaxies. We also provide a linear fit as a function of M_V of the distance out to which dwarfs are detected with each of 50%, 90%, and 99% efficiency. These fits assume an underlying dwarf galaxy population with combinations of sizes and luminosities similar to those known.

2009 will bring about the beginning of the Southern Sky Survey, and with it a way to uniformly search a further 20,000 square degrees of sky for new MW dwarfs. We will apply our algorithm to the incoming data and produce the most complete and well characterized census of the MW neighbourhood possible to date. We may also implement improvements to the algorithm to optimize for stellar streams or young stellar populations. McConnachie et al. (2008) have shown that M31 satellites occupy as yet unexplored size-luminosity space around the Milky Way. Surveys beyond SDSS and SkyMapper, such as Pan-STARRS and LSST, will be needed to carefully search for such systems. Even with our carefully characterized detection limits the true number of MW satellites remains highly uncertain.

We thank Bill Wyatt and the Telescope Data Center at SAO for maintaining a copy of SDSS at the Harvard-Smithsonian Center for Astrophysics. SW thanks the Institute for Theory & Computation (ITC) at Harvard for support and hospitality and the Smithsonian Astrophysical Observatory for financial support during the final stages of this work. Thanks to Pavel Kroupa, Iskren Georgiev, Jose Robles and Charley Lineweaver for helpful comments and discussion. HJ and SW further acknowledge financial support from the Go8/DAAD - Australia Germany Joint Research Co-operative Scheme and through the Australian Research Council Discovery Project Grant DP0451426.

REFERENCES

- Adelman-McCarthy, J. K. et al. 2008, ApJS, 175, 297
 —. 2007, ApJS, 172, 634
 Bailin, J., Power, C., Norberg, P., Zaritsky, D., & Gibson, B. K. 2007, MNRAS, submitted (astro-ph/0706.1350)
 Belokurov, V. et al. 2008, ApJ, submitted (astro-ph/0807.2831)
 —. 2006a, ApJ, 642, L137
 —. 2007, ApJ, 654, 897
 —. 2006b, ApJ, 647, L111
 Brainerd, T. G. 2005, ApJ, 628, L101
 Bullock, J. S., Kravtsov, A. V., & Weinberg, D. H. 2001, ApJ, 548, 33
 de Jong, J. T. A. et al. 2008, ApJ, 680, 1112
 Diemand, J., Kuhlen, M., & Madau, P. 2007, ApJ, 667, 859
 Fukugita, M., Ichikawa, T., Gunn, J. E., Doi, M., Shimasaku, K., & Schneider, D. P. 1996, AJ, 111, 1748
 Girardi, L., Grebel, E. K., Odenkirchen, M., & Chiosi, C. 2004, A&A, 422, 205
 Gunn, J. E. et al. 1998, AJ, 116, 3040
 Hogg, D. W., Finkbeiner, D. P., Schlegel, D. J., & Gunn, J. E. 2001, AJ, 122, 2129
 Holmberg, E. 1969, Arkiv for Astronomi, 5, 305
 Holtzman, J. A., Afonso, C., & Dolphin, A. 2006, ApJS, 166, 534
 Irwin, M. J. 1994, in Dwarf Galaxies, ed. G. Meylan & P. Prugniel, 27
 Irwin, M. J. et al. 2007, ApJ, 656, L13
 Ivezić, Ž. et al. 2004, Astronomische Nachrichten, 325, 583
 Kang, X., Mao, S., Gao, L., & Jing, Y. P. 2005, A&A, 437, 383
 Keller, S. C. et al. 2007, Publications of the Astronomical Society of Australia, 24, 1
 Kleyna, J. T., Geller, M. J., Kenyon, S. J., & Kurtz, M. J. 1997, AJ, 113, 624
 Klypin, A., Kravtsov, A. V., Valenzuela, O., & Prada, F. 1999, ApJ, 522, 82
 Klypin, A., Zhao, H., & Somerville, R. S. 2002, ApJ, 573, 597
 Kposov, S. et al. 2007a, ApJ, accepted (astro-ph/0706.2687)
 —. 2007b, ApJ, 669, 337
 Kravtsov, A. V., Gnedin, O. Y., & Klypin, A. A. 2004, ApJ, 609, 482
 Kroupa, P., Theis, C., & Boily, C. M. 2005, A&A, 431, 517
 Liu, C., Hu, J., Newberg, H., & Zhao, Y. 2008, A&A, 477, 139
 Martin, N. F., de Jong, J. T. A., & Rix, H.-W. 2008, ApJ, accepted (astro-ph/0805.2945)
 Martin, N. F., Ibata, R. A., Chapman, S. C., Irwin, M., & Lewis, G. F. 2007, MNRAS, 380, 281
 Mateo, M. L. 1998, ARA&A, 36, 435
 McConnachie, A. et al. 2008, ApJ, accepted (astro-ph/0806.3988)
 Metz, M., Kroupa, P., & Jerjen, H. 2007, MNRAS, 374, 1125
 Metz, M., Kroupa, P., & Libeskind, N. I. 2008, ApJ, 680, 287
 Moore, B., Ghigna, S., Governato, F., Lake, G., Quinn, T., Stadel, J., & Tozzi, P. 1999, ApJ, 524, L19
 Okazaki, T., & Taniguchi, Y. 2000, ApJ, 543, 149
 Piatek, S., Pryor, C., Bristow, P., Olszewski, E. W., Harris, H. C., Mateo, M., Minniti, D., & Tinney, C. G. 2007, AJ, 133, 818

- Pier, J. R., Munn, J. A., Hindsley, R. B., Hennessy, G. S., Kent, S. M., Lupton, R. H., & Ivezić, Ž. 2003, *AJ*, 125, 1559
- Schlegel, D. J., Finkbeiner, D. P., & Davis, M. 1998, *ApJ*, 500, 525
- Simon, J. D., & Geha, M. 2007, *ApJ*, 670, 313
- Skrutskie, M. F. et al. 2006, *AJ*, 131, 1163
- Smith, J. A. et al. 2002, *AJ*, 123, 2121
- Strigari, L. E., Bullock, J. S., Kaplinghat, M., Diemand, J., Kuhlen, M., & Madau, P. 2007, *ApJ*, 669, 676
- Tollerud, E., Bullock, J., Strigari, L., & Willman, B. 2008, *ApJ*, submitted (astro-ph/0806.4381)
- Tucker, D. L. et al. 2006, *Astronomische Nachrichten*, 327, 821
- Walsh, S. M., Jerjen, H., & Willman, B. 2007a, *ApJ*, 662, L83
- Walsh, S. M., Willman, B., Sand, D., Harris, J., Seth, A., Zaritsky, D., & Jerjen, H. 2007b, *ApJ*, accepted (astro-ph/0712.3054)
- Whiting, A. B., Hau, G. K. T., Irwin, M., & Verdugo, M. 2007, *AJ*, 133, 715
- Willman, B. 2003, PhD thesis, University of Washington
- Willman, B. et al. 2005a, *AJ*, 129, 2692
- Willman, B., Dalcanton, J., Ivezić, Ž., Jackson, T., Lupton, R., Brinkmann, J., Hennessy, G., & Hindsley, R. 2002, *AJ*, 123, 848
- Willman, B. et al. 2005b, *ApJ*, 626, L85
- Willman, B., Governato, F., Dalcanton, J. J., Reed, D., & Quinn, T. 2004, *MNRAS*, 353, 639
- York, D. G. et al. 2000, *AJ*, 120, 1579
- Zentner, A. R., Kravtsov, A. V., Gnedin, O. Y., & Klypin, A. A. 2005, *ApJ*, 629, 219
- Zucker, D. B. et al. 2006a, *ApJ*, 650, L41
- . 2006b, *ApJ*, 643, L103